

California State University, Northridge

Constraining long term slip rates along the San Andreas Fault System using B4 LiDAR and Cosmogenic
Beryllium-10 dating methods at Millard Canyon, San Geronio Pass, California

A thesis submitted in partial fulfillment of the requirements
for the degree of Master of Science in Geology

By
Ian Cody Desjarlais

December 2017

Copyright by Ian Cody Desjarlais 2017

The thesis of Ian Cody Desjarlais is approved by:

Matthew d'Alessio, Ph.D.

Date

Richard V. Heermance, Ph.D.

Date

John D. Yule, Ph.D. Chair

Date

ACKNOWLEDGEMENTS

This work would not have been possible without several past and present CSUN graduate and undergraduate students studying the San Geronio Pass region, all working collaboratively under the leadership of Dr. John D. Yule. His work in the field has yielded many important discoveries which have led to new and greater understanding of the region. Dr. Dick Heermance took me under his wing and with great patience guided me through all the intricacies of the dating methods applied here in this thesis. His guidance helped me work through this long process which included long hours in the lab, data reduction, draft revisions and continued guidance and encouragement through the finish line. I would like to thank the SCEC community for supporting student research in this exciting and important field of study. Their financial support (SCEC Project 12209) provided funding for this research including sample analysis at Lawrence Livermore National Lab. I would like to thank Eshan Ebrahim for taking care of me while I was fighting Valley Fever, and Linda Doran for making a lifesaving batch of her chicken tortilla soup for me after I was hospitalized. Lisa Wolf, Jose Cardona, and Ryan Witkosky for the various ways in which they each helped me to reach the summit of this long and arduous climb. I would especially like to thank Shawna Couplin as she has been involved in most every part of my life since then!

DEDICATION

I would like to dedicate this thesis to my mother who raised me, and for encouraging me to learn by making mistakes. This upbringing set me on the path to lifelong learning for which I will be always walking- and that has made all the difference.

Table of Contents

COPYRIGHT PAGE.....	ii
SIGNATURE PAGE.....	iii
ACKNOWLEDGEMENTS.....	iv
DEDICATION.....	v
LIST OF FIGURES.....	ix
ABSTRACT.....	x
1. Introduction	1
2. Background	4
2.1 Tectonic Setting	4
2.2 Crustal Blocks	4
2.3 Active Tectonic Blocks	5
2.4 Evolution of San Andreas Fault Through Time	6
2.5 Study Area	6
2.5.1 Millard Canyon Drainage	6
2.5.2 Millard Canyon Active Tectonic Features	7
2.5.2.1 Fault Exposure	7
2.5.2.2 Terrace Offset	7
2.5.2.3 Scarps in Holocene Alluvium	7
2.6 Previous Work	
2.6.1 Competing 3D Models	8
2.6.2 Geologic Slip Rates	8
2.6.3 Geodetically Derived Slip Rates	9
2.6.4 Three Dimensional Numerical Deformation Modeling	10
2.6.5 Paleoseismic Studies	10
3.0 Methods	
3.1 Data Acquisition	11
3.1.1 Digital Elevation Data	11
3.1.2 Sample Collection	12
3.2 Cosmogenic Methods	13
3.2.1 CRN Exposure Theory	13
3.2.2 Depth Profile	13
3.2.3 Burial Dating Method	14

3.2.4 Sample Processing	15
3.3 Data Reduction and Analysis	15
3.3.1 Cosmogenic Data Reduction	15
3.3.1.1 Data Reduction - Surface Exposure Samples	15
3.3.1.2 Data Reduction – Depth Profile Samples	16
3.3.1.3 Data Reduction – Burial Samples	16
3.3.2 Calculation of Fault Plane Kinematics	17
4.0 Results	18
4.1 Cosmogenic Ages of Millard Canyon Surfaces	18
4.1.1 Qf4 Depth Profile	18
4.1.2 Qf4 Surface Boulders	18
4.1.3 Preferred Age of Qf4	19
4.2 Burial Samples – Heights Fanglomerate Qh	19
4.3 Scarp Heights Components and Rates	20
4.3.1 F2 Scarp	20
4.3.2 F1 Scarp	21
5.0 Discussion	
5.1 Challenges with Interpretation and Data Availability	22
5.1.1 Evidence of Surface Modification – Qf4 Surface Exposure Samples	22
5.1.2 Evidence of Surface Modification – Qf4 Depth Profile	23
5.1.3 Burial Sample Results – Qh Ages	24
5.1.4 Scarp Height Measurement – Qf4 Continuity Across F2	24
5.2 Estimation of Coseismic Deformation	25
5.2.1 Banning Strand SAF – F1	26
5.2.1.1 Dip Slip per Event	26
5.2.1.2 Net Slip per Event	26
5.2.2 San Gorgonio Pass Fault – F2	27
5.2.2.1 Dip Slip per Event – Undefined Recurrence Interval	27
5.2.2.2 Dip slip per Event – Defined Recurrence Interval	27
6.0 Conclusion	27
6.1 Slip Transfer Through SGP	28
6.2 SGP Fault Team	29
6.3 Potential for Large Magnitude Events	30

References	31
Appendix A - Figures	35
Appendix B – AMS Data	65
Appendix C - Formulas Used	68

List of Figures

Figure 1.1 Index Map	35
Figure 1.2 Geologic Slip Rates and Paleoseismicity Southern San Andreas Fault	36
Figure 1.3 Shakeout Scenario Model	37
Figure 1.4 Azimuthal Variation across southern San Andreas Fault	38
Figure 2.1 Major Crustal Blocks	39
Figure 2.2 Regional Geologic Map	40
Figure 2.3 Millard Canyon Drainage	41
Figure 2.4 Salton Trough Drainage Map	42
Figure 2.5 Tectonic Geologic Map- Millard Canyon	43
Figure 2.6 High Resolution Digital Elevation Products	44
Table 2.1 Compilation of Slip rate data southern San Andreas Fault	45
Figure 3.1 Digital Elevation figure with sample and scarp locations	46
Figure 3.2 Cosmogenic Radionuclide Formation	47
Figure 3.3 CRN Depth Profile Concept	48
Figure 3.4 Cosmogenic Burial Dating Method	49
Figure 4.1 Depth Profile -Qf4	50
Figure 4.2 Linear Regression Analysis	51
Figure 4.3 Statistical Plot Qf4 Surface Boulders	52
Figure 4.4 Probability Kernel Density Plot -Qf4 Surface Boulders	53
Figure 4.5a Scarp Profile Qf4/F2	54
Figure 4.5b Scarp Profile Qf1/F2	55
Figure 4.5c Scarp Profile Qf3/F1	56
Figure 4.5.d Scarp Profile Qf2/F1	57
Figure 4.6 Millard Canyon Longitudinal Terrace Profile	58
Table 4.1 Summary of Kinematic Results	59
Figure 5.1 Millard Canyon <i>Larrea Tridentada</i> Relative Dating Mapping	60
Figure 6.1 Analysis of San Gorgonio Pass Fault trace Azimuth	61
Figure 6.2 Conceptual Geometry for conversion of Contractional motion into strike slip motion	62
Figure 6.3 San Gorgonio Pass Slip Rates through Millard Canyon	63
Figure 6.4 Tectonic Evolution- Millard Canyon Alluvial Fan Geomorphology	64

ABSTRACT

Constraining long term slip rates along the San Andreas Fault System using B4 LiDAR and Cosmogenic Beryllium-10 dating methods at Millard Canyon, San Gorgonio Pass, California.

By

Ian Cody Desjarlais

Master of Science in Geology

Fault scarps cut a series of Holocene alluvial fan surfaces in Millard Canyon, within San Gorgonio Pass (SGP). These fault scarps are likely the result of coseismic slip along the San Andreas Fault system during potentially large ($M_w > 7$) earthquakes. Here I provide a new age for Holocene surface Qf4, mapped by Yule and Sieh (2003). Charcoal fragments beneath Qf2 limits the surface to 1270 ± 80 years before present (ybp) and new ^{10}Be exposure data provides age constraints of 4800 ± 1600 ybp for Qf3 and 6800 ± 550 ybp for Qf4. These new ages provide limits on the timing of slip through San Gorgonio Pass. Airborne LiDAR from the B4 dataset was used to identify and measure preserved scarps that cut the terrace surfaces. The northernmost fault (F1) is a 45° north dipping active oblique strike slip thrust fault that vertically offsets units Qf2 and Qf3 by 1.8 ± 0.1 m and 3.1 ± 0.7 m respectively. The southern fault (F2), a 25° north dipping active thrust fault vertically offsets units Qf1 and Qf4 by 1.9 ± 0.2 m and 12.7 ± 1.4 m respectively. I mathematically resolve these vertical throw components into a set of fault plane kinematics and rates including uplift rate, dip slip rate and contraction rates using the new age constraints. I then interpret likely per event slip rates on each fault by incorporation of known recurrence intervals for faults in Millard Canyon (McBurnett, 2011). The northern fault F1 is shown to have a long-term dip slip rate of 2.0 ± 0.1 mm/yr and an interpreted per event net slip of 2.8 ± 0.3 meters. The southern fault shows evidence of primarily dip slip at a rate of 4.4 ± 0.6 mm/yr and a per event dip slip rate of 2.2 ± 0.3 meters. Summation of this local SGP slip yields 6.4 ± 0.6 mm/yr for the Holocene dip slip rate through SGP. Summation of the observed uplift yields 3.3 ± 0.3 mm/yr through the Holocene. These faults are the primary conduit for slip through SGP and are interpreted to release interseismic strain during large magnitude earthquakes of $M_w > 7$ (Yule and Sieh, 2003).

1. Introduction

In the early 1900's earthquake geology was just a burgeoning scientific field, relying mostly on written account of earthquakes, and when available oral histories. It wasn't until the actualization of the massive destruction yielded by the 1906 San Francisco earthquake, that North American geologists were firmly resolved to uncover and understand the geographic extent of the fault network that was capable of such a disaster. Harold Fairbanks along with a team of scientist associated with U.C Berkeley spearheaded efforts to trace the southern extent of the 1906 surface rupture near San Juan Bautista, California (Hough, 2010). After successfully locating the southern terminus, Fairbanks and his team continued the charge southward. Following geomorphic surface features indicative of faulting, the team navigated through the California coastal ranges, Carrizo plain region, and San Gabriel Mountains, enduring what was presumably rough terrain, austere living conditions, and a range of temperature extremes. After painstakingly tracing the fault roughly 300 miles from San Juan Bautista, the team was finally confronted with the only insurmountable challenge of their journey, one that put a stopping point to their endeavor. That obstacle was the San Gorgonio Pass (SGP). The formidable SGP region, although not physically unnavigable, presumably provided far too many fault-tracing challenges which would have impeded Fairbanks efforts to successfully map the fault (Figure 1.1). After a long journey and exhaustive effort, Fairbanks concluded in defeat "it is probable that a fault continues on still farther along the mountains lying north of the Salton Basin." (Hough, 2010). The ability of the SGP to obfuscate such an ambitious group of scientists is a testament to the complex and at-times esoteric geologic nature of the region that has now been studied by many groups and individuals for over 100+ years and has been designated a Special Fault Study Area (SFSA) by the Southern California Earthquake Center (SCEC) since 2012.

Early work in the SGP region brought attention to the extreme topographic expression of prominent linear ridgelines and valleys, as well as the lack of lateral stream offset (Noble, 1932; Allen, 1957). To this day, geomorphic expression of deformation features serve as the backbone of fault studies, providing the primary evidence of motion that is visible on the surface. Sections of the San Andreas Fault (SAF) known to display continuous slip such as the Carrizo Plain section produce offset fluvial channels such as that observed near Wallace Creek (Figure 1.2) which provide unequivocal evidence of strike slip motion (Sieh and Jahns, 1984). At Wallace Creek, the fault manifests on the surface as a single fault strand, centralizing shear slip onto a single, relatively

simple fault surface. Within these types of zones, it is believed that simple geometries, high heat flow, and higher fluid pressures modulate the resistance to shear stress, thereby allowing for frequent, perhaps continuous slip to accrue along these strike-slip “straightaways.” Within the major step-overs such as the Tejon Pass or SGP, it is inferred that higher shear stress resistance exists due to complex geometries and lower heat flow (Sykes and Seeber, 1985; Yule and Sieh, 2003). One might speculate that whereas the creeping sections with low shear resistance yield more frequent, smaller intensity earthquakes, the inverse may be true for the locked step over zones. Could it be that these locking sections (step overs) are capable of accumulating greater quantities of interseismic strain, presumably released as infrequent-large magnitude ruptures? The powerful 1857 M_m 7.9 Fort Tejon earthquake may provide a suitable analog for the magnitude of event that could be expected to result from rupture of these step over zones. Sykes and Seeber,(1985) suggest that as a result of the 1857 Fort Tejon quake, the SGP knot is at present in a relatively more advanced stage of strain accumulation than nearby Tejon Pass and is therefore more prone to rupture.

Throughout the trace of its surface expression from Parkfield in the north to the Salton Trough in the south, the southern San Andreas Fault Zone (SSAFZ) displays a wide range of coseismic and interseismic behavior. Changes in azimuth direction (Figure 1.4) of the surface trace of this major dextral strike slip fault in conjunction with the variations in subsurface geometries directly effects rates of crustal deformation and earthquake size. The SGP area of the SAF Big Bend zone has therefore been the subject of many studies (Allen, 1957; Matti and Morton, 1993; Yule and Sieh, 2003) as the effects of the “Big Bend” on seismicity are not fully understood. Application of geophysical methods (Langenheim et al., 2005 and references therein) to interpret subsurface geometries show two results. First, shallow north-dipping thrusts (ancestral Banning Fault) are observed to link with the San Gorgonio Pass Fault at depth. Second, at depths greater than 5km, crustal deformation within SGP is complex and partitioned to strike slip and thrust faults, which serve to decentralize the slip from the master fault (Jones et al., 1986; Seeber and Armbruster, 1995; Magistrale and Sanders, 1996; Carena et al., 2004). What are the implications of this structural complexity through the SGP? Does geologic data show record of recent through going ruptures? What is the frequency and magnitude of seismic events in the SGP region and when might the next big one be? Is a San Gorgonio Pass rupture capable of producing a Shakeout Scenario (M_w 7+) earthquake (Figure 1.3)? Millard Canyon within the SGP is a premier study area to develop and test these hypotheses due to the presence of two observably active faults, each presumably recording slip activity within Holocene alluvium (Yule and Sieh, 2003).

As recently as 125kya, regional shifts in tectonic forces began directing high rates of strain accumulation through SGP (Matti and Morton, 1993; Yule and Sieh, 2003). It is believed that through time, this strain has manifest as the San Gorgonio Pass Fault, an active oblique reverse tear fault showing evidence of rapid vertical offsets throughout the Holocene (Yule and Sieh, 2003). In addition to the interpreted movement on the San Gorgonio Pass Fault, evidence shows what may be the reactivation of the adjacent ancestral Banning Fault. The ancestral Banning Fault represents the transform plate boundary between the North American and Pacific Plate (Matti and Morton, 1993; Langenheim et al., 2005). Believed to have accommodated much of the transform boundary plate motion as slip during the late Miocene, it was subsequently “deactivated” due to what may have been complex strain partitioning to other faults in the slip regime of the southern San Andreas Fault Zone(SSAFZ) such as the San Jacinto Fault and Eastern California Shear Zone (ECSZ). This reactivated oblique slip fault is presently referred to as the Banning Strand of the San Andreas Fault. The rates of slip on the family of faults within the SSAFZ should be correlated, perhaps inversely as they work together as a system to partition shear stress as slip through the SGP region. This study aims to construct a working model of long term slip rates for faults within SGP during the Holocene, using a multifaceted approach involving field mapping, cosmogenic age dating of alluvium, and analysis of remotely sensed elevation and imagery data.

2. Background

2.1 Tectonic Setting

Throughout the late Cenozoic, plate boundary forces between the subducted Farallon plate, Pacific plate, and North American plate have been applying a complex pattern of stress regimes to regional and local crustal blocks permanently modifying the geography of southern California (Atwater, 1970). This deep crustal motion resulting from the transform plate boundary between the Pacific and North American plates is driving surface processes which overlay and imprint a complex geomorphic record of the active regional tectonics of the area (Figure 2.1). The temporal and spatial dynamics of major crustal blocks in southern California have created a stunning landscape of high-relief topography, predominantly characterized by the east-west trending Transverse Ranges of southern California (Figure 1.1). At the eastern extent of the Eastern Transverse Range (ETR) province is the San Geronimo Pass (SGP) region, a pass that is bordered by the southern San Bernardino Mountains and northern Peninsular Ranges. In the vicinity of the SGP, the southern San Andreas Fault Zone (SSAFZ) splits into multiple strands, each of which accommodate or have accommodated slip at varying rates since inception of the Gulf of California between 6-10 Ma (Oskin et al., 2001; Oskin and Stock, 2003). Matti and Morton, (1993) suggest that throughout the last 5 Ma, the SAFZ has, by mechanisms not fully understood, migrated its active strand geographically by preferentially activating one strand and deactivating another, further complicating the reconstruction and interpretation of this geologically intricate study region.

2.2 Crustal Blocks

The major crustal blocks underlying the SGP have been well defined spatially and lithologically by Langenheim et al., (2005). The three key players are the San Bernardino Mountains block (SBMB), Peninsular Range Mountain block (PRMB) and San Gabriel Mountains block (SGMTB; Figure 2.1). These three crustal blocks all of which are intersected by late Cenozoic faulting associated with the SAFZ, undergo a complex interplay of forces and rock mechanics filling structural roles in the tectonic evolution of the SGP study area up to the present-day. In their work, Langenheim et al., (2005) conclude that the ancestral Banning Fault represents the crustal boundary between the Transverse and Peninsular Range basements and once linked with the San Gabriel fault to the west in the San Gabriel Mountains (Figure 2.1). Their interpretation of gravity, aeromagnetic, and seismic data at

this boundary supports evidence for a tectonic wedge of Peninsular Range basement rocks above Transverse Range basement, which adds to the complexities of the SGP region.

2.3 Active Tectonic Blocks- Evidence of Active Long-term Uplift within San Gorgonio Pass Region

The active tectonic blocks of SGP are defined by differences in respective 3D kinematics, determined by evaluation of geomorphology and relative cooling histories (Spotila et al., 1998). The crustal San Bernardino Mountains block is cut by numerous northwest-southeast striking curvilinear faults resulting from recent (last ~5 Ma) changes in the locations of the active strands of the SAFZ (Spotila et al., 1998). The block itself is comprised of 4 smaller blocks (active tectonic blocks), namely Big Bear Block (BBB), San Gorgonio Block (SGB), Yucaipa Ridge-Wilson Creek Block (YRWCB) and the Morongo Block (MB). Spotila et al., (1998) categorizes and describes the tectonic histories of each block in great detail. Their application of apatite helium thermochronometry allowed for determination of the rates of uplift of independent blocks. Their study relied on the variations of topographic elevation between each adjacent block and the geomorphic evidence that these blocks were, and are uplifting at different rates. Their work provides evidence for the conversion of dextral slip into vertical motion on the Mill Creek fault over the last 1.6 Ma.

The conceptual model adopted in this (Millard Canyon) study suggests uplift within the SGP may be caused by geometry of the contractional fault stepovers and/or restraining bends there (Matti et al., 1985; Yule and Sieh, 2003). Yucaipa Ridge (YR) is northwest of a 15km wide stepover between the San Bernardino Strand SAF and Coachella Valley Strand SAF. A palinspastic reconstruction of the nearly 8-10km of slip known to have occurred during the Pleistocene (Matti et al., 1985) places YR closer to the stepover. In this case uplift would be the result of ramping up on contractional structures such as the San Gorgonio Pass Fault (Allen 1957, Matti et al. 1985). Apatite helium ages of Spotila et al., (1998) for the YR and WC blocks (0.7-1.6 Ma) indicate rapid cooling, which suggests uplift of the SBMs has occurred relatively rapidly because of thrusting and oblique slip through complexities in SAF/SGP. This conclusion is led by the assumption that uplift generated by slip on the shallow dipping North Frontal Thrust System would manifest slower than that generated by slip along the steep-dipping faults of SGP.

2.4 Evolution of SAF Geometry Through Time

During the late Miocene, dextral slip on the ancestral Banning Fault between the Peninsular Range Mountains block and San Bernardino Mountains block dominated the slip regime by accommodating a large percentage (possibly most or all) of strike-slip shear along the transform plate boundary. The early Pliocene brought the development of the San Andreas Fault Zone (SAFZ) including Wilson Creek and Mission Creek strands (Figure 2.1). The most recent stage of development is characterized by the complex decentralization of slip onto newly developing strands. Matti and Morton (1993) identified three key geologic events originating in the Quaternary responsible for fostering the complex structure of the SGP and surrounding region today. First, a 20km wide left-step over on the Mission Creek fault north of the SGP formed ~1.5Ma. Around 1 Ma, the inception of strike slip motion along the San Jacinto Fault to the west of SGP then began out of necessity, as the SGP from then to the present is effectively hastening regional slip transfer. This accommodation allowed the regional shear stress to be diverted around the SGP structural knot; essentially a “slip detour”. This fault trends towards the Mojave Section SAF, however its surface trace has not been observed to connect with it (Matti et al., 1985). At approximately 125kya, the onset of contemporaneous contraction within the SGP formed a left step over (Figure 2.1) manifesting as thrusts and tear faults (present day San Gorgonio Pass Fault) (Matti et al., 1985; Yule and Sieh, 2003). This slip regime describes the known state of the fault system up to and including the present-day configuration.

2.5 Study Area

2.5.1 Millard Canyon Drainage

With its northern upstream extent being the Mission Creek Strand San Andreas Fault (MCSSAF), the Millard Canyon drainage basin (HUC-12-181002010104) encompasses an area of roughly 43km² (Figure 2.3). Geomorphic analysis by McGuire (2011) indicates the average slope within the Millard Canyon drainage basin is 26.9 degrees. McGuire (2011) estimates an average basin-wide ¹⁰Be spallogenic production rate of roughly 12.9 atoms g⁻¹ yr⁻¹. The CRN production rate of the upper zones is nearly twice the in-situ production rate found at the elevation of the Millard Canyon alluvial fans I investigate in this study.

Of great pertinence to this slip rate study is McGuire’s finding of consistent values of ¹⁰Be within the active channels of Millard Canyon wash. The exhaustive analysis of grain size and CRN concentrations by McGuire (2011)

shows the active channel of Millard Canyon to have relatively low ^{10}Be concentrations ranging on the order of 7,830-14,900 atoms per gram of quartz. The average of these values is ~10,000 atoms per gram of quartz and represents an erosion and transport time of 1000-2000 years, which I use as a baseline in this study to corroborate my independently derived inheritance values (see results section).

2.5.2 Millard Canyon Active Tectonic Features

2.5.2.1 Fault Exposure

Considered inactive in other localities, the Banning Strand SAF shows clear evidence of activity where a 3 km long section intersects Millard Canyon within SGP (Figure 2.5). Evidence of contractional slip-accrual manifests as a suite of channel-fill terraces and thrust scarps offsetting late Quaternary to Holocene alluvium. Exposed within the eastern wall of Millard Canyon, the Banning Strand is exposed showing a $\sim 45^\circ$ N dipping fault surface (Yule and Sieh, 2003). This fault has accommodated the thrusting of crystalline rocks on top of Pleistocene conglomerates (Qh) which are present in the hanging wall and footwall respectively (Yule and Sieh, 2003). Exposed within the western terrace riser wall of the active channel, the San Geronimo Pass Fault is observed to be dipping $\sim 24^\circ$ in a northerly direction (Yule and Sieh, 2003).

2.5.2.2 Terrace Offset

On the canyon floor, the active and abandoned channels of the drainage system imprint an elegant suite of alluvial terraces (Figures 2.5 & 2.6). Work by Yule and Sieh (2003) show dextral and vertical offset components of a Holocene terrace riser across F1 of ~ 4.5 and 2.5 meters respectively. This shows the component of local dextral strike slip to be ~ 2 times greater than the vertical component (Yule and Sieh, 2003). Terrace material (Qf2 of Yule and Sieh, 2003) was dated with radiocarbon methods by McBurnett (2011) providing an age of $\sim 1270 \pm 80$ yrs. As Qf1 is spatially inset into an erosional feature within Qf2, it must have an age younger than Qf2 (Figure 2.5). Using these dimensions and preferred age of Qf2, a rough estimate of lateral terrace offset rate is ~ 4 mm year.

2.5.2.3 Scarps in Holocene Alluvium

Within the Millard Canyon Fan, two active faults cause vertical offsets of Holocene Alluvium (Figure 2.5 & 2.6). The re-activated Banning Strand (Yule and Sieh, 2003) causes offset alluvium in the northern portion of the

study area, from here on referred to as F1. Deformation on the San Gorgonio Pass fault is responsible for the scarp formation observed just beyond the southern extent of the canyon, from here on referred to as F2. Yule and Sieh (2003) employed a total station survey to make surface profiles across the F1 and F2 scarps observed to deform the Holocene mapping units (Qf1, Qf2, Qf3, Qf4). Their survey data across F1 show 5.2 ± 0.7 m and 2.5 ± 0.7 m scarps in Qf3 and Qf2, respectively. At F2, ground survey data shows 12.6 ± 0.7 m and 1.5 ± 0.1 m scarps in Qf4 and Qf1, respectively. I present additional scarp profiles here (Section 4) that are derived from the B4 LiDAR data. The greater relative scarp heights of Qf4 and Qf3 fundamentally implies these surfaces are older as they have recorded more cumulative slip than the (younger) Qf1 and Qf2 material, thereby validating the observed relative dating of these surfaces.

2.6 Previous Work

2.6.1 Competing 3D Models

Hypothetical models of Seeber and Armbruster (1995) suggest that the San Gorgonio Pass actively offsets the surface trace of the SAF from its continuous fault-plane equivalent at depth, i.e. what is visible on the surface does not represent what is in the subsurface. Rasmussen and Reeder (1986) describe what they evaluate to be a mega-landslide effectively covering up the surface trace of the SAFZ. Multiple other studies have shown that a continuous fault plane does not extend through the SGPFZ connecting the San Bernardino Strand SAF and Coachella Valley Strand Banning Fault (Noble, 1932; Allen, 1957; Matti and Morton, 1993; Yule and Sieh, 2003; Carena et al., 2004; Magistrale and Sanders, 1996). This latter group interprets the SGP stepover region to be a complex contractional system of strike slip, tear and oblique thrust faults which are laterally discontinuous and which transfer the dextral component of shear slip for the region.

2.6.2 Geologic Rates of Slip

Geologically-derived rates of slip for the SSAFZ are determined by strategic and systematic study of surficial deposits found adjacent to actively deforming regions. Table 2.1 provides a comprehensive list of previous slip-rate studies from the SSAFZ. Studies incorporated trenching perpendicular to active faults to directly observe offset stratigraphic markers and piercing points that record slip vectors. An alternate approach relies on

characterizing slip that occurs subsequent to the deposition of surface alluvium, such as abandoned or inactive sections of an alluvial fan, which may yield surface rupture creating a scarp. In arid environments, scarps may remain fresh in appearance for years, compared to scarps in less arid environs that are subject to relatively rapid degradation through weathering. Preserved scarps can be quantitatively characterized using surveying methods and by measuring total vertical component of offset between the once-continuous surface. In study areas where the only component of motion is strike slip, the measured lateral offset of a piercing line such as an offset stream channel or perhaps even man-made features such as fence post will provide an accessible method of determining slip. In this text, I refer to geologic slip rates as data obtained using these approaches. These rates are different from geodetically derived rates as they are the result of direct observations of ground movement.

2.6.3 Geodetically Derived Rates of Slip

With the advent of satellite-based geodetic methods over the recent decades, the relative kinematics of crustal blocks can be determined. This method tracks the motion of fixed, ground-based monuments over time with respect to a stable reference matrix, e.g. "Stable North American Plate". Resolution of differences in crustal velocities across known fault geometries will provide a geodetically derived slip rate. Although this data depicts actual movement of the crust, many complications arise due to the presence of strike slip, thrust, and oblique-reverse faulting, all of which are frequently observed in southern California. According to Spinler et al., (2010) application of geodetic methods along plate margins such as SSAF is complicated by frequent coseismic displacements, poorly characterized rheology of crust, and complex geometry of crustal fault systems. Adding to that, acute-elastic rebound subsequent to earthquake events may likely drown the long-term kinematic rates that exist in an area. For example, if one takes two steps forward, then one step back, it may appear to an onlooker as though the individual took only one step forward. It is difficult to assign surface velocities of geodetic monuments across complex networks of faults as the elastic strain fields tend to overlap and obfuscate their vector signal.

Aside from these inherent difficulties, the use of geodetic deformation models to evaluate interseismic elastic loading between earthquakes can potentially be very much complementary to geologically-determined rates such as those determined in this study. These two methods can be combined to determine the rate at which slip accrues which is directly linked to frequency and magnitude of past and future earthquakes (Spinler et al. 2010).

(See Table 2.1) In other words, the rate of interseismic elastic strain accumulation is (or should theoretically be) roughly equivalent to the amount of slip expressed during earthquakes

2.6.4 Three-Dimensional Numerical Deformation Modeling

A common misconception about strike slip fault systems is that the fault plane exists in near-vertical orientation. Supporters of the contractional left stepover model (1908; Noble, 1932; Allen, 1957; Matti and Morton, 1993; Yule and Sieh, 2003; Carena et al., 2004; Magistrale and Sanders, 1996) argue that in fact the SAF passes through SGP in a north-dipping orientation. Efforts have been made to investigate the feasibility of this orientation using three dimensional numerical models of active deformation within SGP region. In-depth models using Boundary Element Method show strong evidence that the SAF takes on a north-dipping configuration as it wends its way through SGP region. In their model, Dair and Cooke (2011), made a comparison between the long-term effect on deformation in a scenario where the SAF is vertical, and where it is dipping to the north. The results of these iterations showed uplift behavior similar to that observed empirically using geologic methods. The results of their model favor the north-dipping orientation of the fault through SGP.

2.6.5 Paleoseismic Studies

As a result of previous works, the alluvial material within Millard Canyon has (limited) age data resulting from radiocarbon dating of charcoals obtained from trenching work performed by McBurnett (2011). In these trench studies, material beneath the surfaces were dated, providing an interpreted age maximum. This existing data validates and reinforces the new data of this study and together provide the foundation for complimentary high and low age constraints on the tectonic/climatic history of the study region.

McBurnett's data represents activity on the northern fault (F1) and is presently the most complete paleoseismic record available for Millard Canyon. His record shows the most recent seismic event at approximately 675 ± 175 years, the penultimate event at 1270 ± 85 years, and another event at $\sim 2000 \pm 700$ years. In this study I will refer to these and other San Gorgonio Pass seismic events using the nomenclature of EI(675 ± 175), EII(1270 ± 85), EIII($\sim 2000 \pm 700$)...etc., the roman numerals representing sequence beginning with the most recent event (EI).

3. Methods

3.1. Data Acquisition

3.1.1 Digital Elevation Data

In this study I used B4 aerial LiDAR data to analyze scarp features within the Millard Canyon Fan in the vicinity of Cabazon, CA. This LiDAR dataset was obtained in 2005 as part of the National Center for Airborne Laser Mapping (NCALM) B4 Project to map the southern San Andreas and San Jacinto faults. Point cloud data was obtained from opentopography.org and assembled into QT Modeler V8.02 software developed by Applied Imagery. This software allowed for active mensuration and manipulation of the LiDAR data set in 3D. Within this modeling environment I characterized fan morphology and the extent of faulting by measuring scarp heights and terrace relationships.

Scarp height measurements were collected by first determining location and azimuth of maximum fan-surface offset and preferred scarp transect location respectively. This effort involved first performing a pre-analysis of LiDAR slope maps to identify the steepest scarp faces, which presumably represent the most well-preserved facet of the scarp. Next, transects were plotted using an adaptive-width swath which allows for a more representative characterization of the scarp, instead of simply using a line. Transect line widths were dependent upon available surface area at each respective scarp; with of a goal of maximizing the area of swath coverage. For example if an offset surface allowed for a 3m wide swath, this would “capture” all point cloud ground returns 1.5 meters on either side of the transect survey line. Each transect was then plotted on a 2 dimensional profile with the elevation on the y-axis and lateral distance along the x-axis. The vertical component of displacement at the fault scarp (throw) was determined as the vertical distance between the footwall and hanging wall, the latter extrapolated down-slope so that it was above the footwall. I collected a series of 10 throw measurements to determine the uncertainty in each measurement which will serve as the foundation for the cascade of calculations made in this study.

LiDAR point cloud data was also used to generate a suite of high-resolution raster DEMs to study the geomorphology of the study area. Rasterized point clouds were imported into open source QGIS Brighton v2.6 and were processed using Raster Terrain Analysis GDAL (Geospatial Data Abstraction Library) plugins and the GRASS open source raster processing modules. The high resolution DEMs facilitated the generation and extraction of

contour maps with contour intervals of 0.25 m. Detailed slope maps of the study area were made to aid in evaluation of scarp location, and to characterize areas of erosion (Figure 2.6). Traces of surface channels (rivulets) were mapped in a vector layer and spatially evaluated. This information was used to understand the formation of the present-day surfaces found in Millard Canyon and surrounding areas.

3.1.2 Sample Collection

The geomorphology of the Millard Canyon Fan area was evaluated and several key surfaces were identified as candidates for Cosmogenic Radionuclide (CRN) sampling. These surfaces are as follows: Qf1, Qf2, Qf3, Qf4, and Qh (Figure 2.5) (Yule and Sieh, 2003). Qf4 is mapped and interpreted as the oldest surface of the current Millard Canyon fan. At the lower fault (F2) this surface is offset vertically by over 12 m (See Results sections). Establishing an age estimate for this surface will effectively extend the temporal range of the slip rate calculations (i.e. the denominator) which is important to understanding how the slip rates change over time (Spinler et al., 2010).

In-situ boulder samples were obtained from the unit mapped as Qf4 by Yule and Sieh (2003) within Millard Canyon (Figure 3.1). The orientation of the exposure face was recorded, as well as the approximate thickness of the sample, as this plays a role in the evaluation of CRN dates. Lastly, a clinometer and pocket transit was used to record the azimuth and inclination of the horizon in ~20 degree segments for 360 degrees radially from the site. This data is used to quantify the degree of cosmogenic ray “shielding” the local mountains have provided to the samples (Balco, 2008). These effects, in conjunction with the effects of the geomagnetic latitude determine the site-specific parameters which enable the interpretation the data (Balco, 2008; Gosse and Phillips, 2001).

The next component of sample collection involved obtaining samples for a depth profile from a soil pit excavated at a site between F1 and F2 within the lateral extent of the Qf4 surface (Figure 3.1). The depth profile required excavation of a trench 1.5 meters in depth from which samples were obtained at depths of 7, 35, 75, 105, and 145 cm beneath ground surface (bgs) (See figure 4.1). The final group of samples obtained were from a depth of 23 m beneath the Heights Fanglomerate (Qh) (Figure 3.1) terrace, bounding the eastern edge of the Millard Canyon Fan. A total of 6 cobbles, 20-40 cm in diameter were taken from a fluvial bed now presently exposed in the eastern wall of Millard Canyon. These samples were targeted to find a constraint on maximum age of the Qh surface, an abandoned paleo fan surface of Millard Canyon.

3.2 Cosmogenic Methods

3.2.1 CRN Exposure Theory

The premise of Cosmogenic Nuclide dating is that mineral crystals exposed at or near the Earth's surface are continuously bombarded by two distinct nuclear particles, neutrons, and to a lesser degree, Muons (a type of Lepton) (Ivy-Ochs et al., 2013; Figure 3.2). The process begins in outer space, where Nucleons (primarily protons) propagate towards earth from many distant sources such as supernovae or coronal mass ejections from the sun. These *primary cosmogenic rays* bombard the upper protective atmosphere of earth, causing a cascade of secondary spallation reactions to occur. (Figure 3.2) The proton bombardment of atmospheric Oxygen and Nitrogen yields a second group of nuclear particles including neutrons (n^0), muons (μ), positrons (β^+), and pions (π), which are referred to as “secondary cosmogenic rays.” These secondary cosmogenic rays continue through the atmosphere eventually bombarding materials on the earth surface, in this case, silica-rich material. The effect of this bombardment is the nuclear modification of ^{28}Si to ^{26}Al , and ^{16}O to ^{10}Be , the end products of which are referred to as cosmogenic nuclides (Ivy-Ochs et al., 2013). These nuclides are produced at a set local rate (production rate) and therefore yield a hidden record of cumulative exposure (as increasing ^{10}Be or ^{26}Al concentration), which if measured can serve as a proxy of exposure time (Lal, 1991). The effect of muogenic radiation is less significant, but muons penetrate much deeper into the surface than neutrons and will impart an exposure signal albeit one less pronounced (Figure 3.2 & 3.3). Muogenic modification of isotopes occurs by the process of negative muon capture. See Gosse and Phillips (2011), and Lal (1991), for a thorough discussion of CRN theory.

3.2.2. Depth Profile

A key objective to many cosmogenic nuclide studies involving sediments is the determination of the presence or absence of cosmic ray *dose inheritance* in the sample media. Inheritance is used to describe a pre-existing exposure of the sample to CRN's imparting what could be considered isotopic “contamination” to the sample. The extent of this “contamination” can be quantified with the use of depth profiles which require the collection samples at a set interval up to 3 m beneath ground surface, considered maximum depth of neutron bombardment (Rood et al., 2011b; Devecchio et al., 2012 and sources there in). In-situ cosmogenic production of

^{10}Be and ^{26}Al will attenuate naturally with depth in an undisturbed clastic (alluvial) sample (Ivy-Ochs et al., 2013). This is due to the preferential absorption of neutrons in the upper-surface quartz grains, thereby diminishing the downward migration of neutrons through the sediment section. This decrease is represented in a plot of depth versus ^{10}Be concentration in Figure 3.3. Theoretically, for material with zero “inheritance,” the ^{10}Be concentration N should approach 0 atoms per gram of Quartz at or near 3 meters depth. If however, at this depth a concentration of ^{10}Be exists, this quantity may be interpreted as the exposure inheritance. Exposure inheritance is the result of CRN production in the sample material during its transport through the drainage basin.

3.2.3 Burial Dating Method

Siliciclastic particles exposed to spallogenic bombardment at or near the surface will accrue cosmogenic nuclides. Subsequent burial of this particle within alluvium, snow or ice, will retard further development of Cosmogenic nuclides in this sample. Burial by alluvium at depths greater than ~3 meters will completely stop spallogenic production of cosmogenic nuclides as neutrons cannot effectively penetrate beyond this depth (Figure 3.4). At the time of deposition, there should theoretically exist a ratio of 6.75 : 1 of ^{26}Al to ^{10}Be (Gosse and Phillips, 2011). Differences in the radioactive decay rates of ^{26}Al and ^{10}Be serve as the chronometers that support the theory behind burial dating methods. Over time, the buried material loses CRN's at a rate determined by the half-lives for ^{26}Al and ^{10}Be , $7.17\text{E}05$ and $1.39\text{E}06$ years respectively. When the burial sample is later collected and subsequently processed for AMS analysis, the quantities of ^{26}Al and ^{10}Be per gram can be determined. These quantities can then be used to calculate the burial age using the sequence of formulas shown in figure 3.4 (Balco and Rovey, 2008). The result of this calculation should provide a number representing the number of years (in years) since the material was buried. Possible errors may arise if the transport history of sampled material is in fact more complex than is initially assumed. For example, material that has been buried, reworked, and then deposited and buried again may have a $^{26}\text{Al}/^{10}\text{Be}$ ratio that does not represent the true depositional/exposure/burial history of the sample. This may cause the burial method formula to yield imprudent ages that do not represent geologically accurate dates, e.g. negative ages. Errors in processing and analysis of ^{26}Al are also frequently problematic and may easily lead to errors in dating such as infeasible ratios of ^{26}Al to ^{10}Be . This will be discussed further in Results section.

3.2.4 Sample Processing

All samples collected were processed at CSU Northridge Rock Research Lab in Northridge, CA. Boulder samples were crushed, and then sieved to obtain the 250-500 micron grain size fraction, yielding approximately 400g of useable material per sample. The second phase of sample processing includes quartz-separation procedures which involved exposing the samples to a systematic regimen of heated acid baths. The first step included 24-hour heated baths in 18% Hydrochloric acid to remove trace organics. Samples were then individually dispensed into 4 L Nalgene HDPE bottles filled with a specified acid solution and placed on heated rollers for 10 -12 hours. The samples underwent a 2% solution bath of HF/HNO₃, and then two 1% baths, magnetic mineral separation with a Frantz machine, and then one final 1% HF/HNO₃ bath. Between each acid wash step, samples were rinsed, dried and subsequently massed. Partial sample aliquots (PSA's) of these quartz separates were sent to University of Colorado Laboratory for Environmental and Geological Studies (UCLEGS) for elemental analysis. After validating the quartz purity utilizing the Al concentration of the PSA samples as a proxy, the complete sample was then digested in concentrated HF on hotplates for 24 hours. Total sample aliquots (TSAs) were obtained from all samples after digestion. The sample residue was then dissolved in acid and separated with two-stage ionic column chemistry techniques to remove unwanted elements such as Iron, Magnesium, Cobalt, and Titanium. Resultant BeOH and AlO residues were then combusted in a fume hood in a quartz crucible to form the Aluminum and Beryllium Hydroxides that were packed into sample targets in a fume hood at CSUN. Samples were sent to Lawrence Livermore Center for Accelerator Mass Spectrometry (LLCAMS) in Livermore, California.

3.3 Data Reduction and Analysis

3.3.1 Cosmogenic Data Reduction

3.3.1.1 Data Reduction- Surface Exposure Samples

AMS data returned for the samples underwent a sequence of data reduction and statistical analysis to determine the ages of the exposure samples. Raw ¹⁰Be/⁹Be AMS ratios were corrected for Boron and background levels and then converted to ¹⁰Be concentrations to 1 σ (atoms g⁻¹) (Balco et al., 2008). The ¹⁰Be concentrations

(Appendix B) were transformed into exposure dates using the CRONUS online exposure calculator (Balco et al., 2008).

Statistical data validation was performed to determine if the individual boulder ages were prudent or improbable. This practice helps to identify outliers which may skew the ages of the boulders. Such data outliers may either be the result of problems in sampling procedures/selection, transport histories, boulder re-mobilization and or spatial re-arrangement (such as rotation in place), surface inflation/deflation, or any of the other variables which may have played a part in the history of the boulder. To evaluate the margin of error associated with the dating technique, normal distributions of the age probabilities were used to find synergistic probability-overlap in order to constrain the most statistically prudent age. Devecchio et al., (2012) and Rood et al., (2011b) use these “camel plots”, essentially smoothed histograms to analyze age frequency probabilities of terrace surface exposures (Balco, 2008). Isoplot v4 was used to calculate mean weighted averages of the independent boulder sample ages as it weighs the respective errors of the individual samples (Leo, 1992).

3.3.1.2 Data Reduction- Depth Profile Samples

The sample AMS data returned from the depth profile was reduced to obtain ^{10}Be concentrations (atoms/gram of quartz) which were plotted versus depth to construct a depth profile plot. Comparisons between ideal subsurface decay curves (zero inheritance) (Figure 4.1) were performed and the results were analyzed. (See Discussion section). This depth profile, (Figure 4.1) which represents data obtained within the Qf4 surface area is intended to provide a surface age as well as inheritance values for the Millard Canyon (MCAN) fan surface. These values were then compared to established inheritance values for the MCAN determined by McGuire (2011). McGuire used CRN methodology to effectively determine erosion and inheritance rates within the MCAN drainage system. Her work showed a ^{10}Be inheritance of nearly 10000 atoms per gram of quartz. To determine an “age” for the depth profile, I apply linear regression of the depth profile samples after Devecchio et al., (2012). The slope of the linear regression line, divided by the production rate is the age of the surface.

3.3.1.3 Data Reduction- Burial Samples

AMS data yielded from the burial samples (1301) included ratios for both $^{26}\text{Al}/^{27}\text{Al}$ and $^{10}\text{B}/^9\text{Be}$. AMS ratios were reduced to isotopic concentrations (atom/gram) according to methods of Balco et al., 2008. The respective concentrations of ^{26}Al and ^{10}Be for each sample were then used to calculate burial ages based on the methods of Balco et al., (2008; See formulas Figure 3.4).

3.3.2 Calculation of Local fault plane kinematics

The foundation of this investigation is the quantification of the observable vertical offset (throw) manifested as scarps in Holocene alluvium. The quantification of this offset is performed using LiDAR point cloud mensuration, in which the result is a scalar value along the vertical "z" axis. If the dip angle of the fault responsible for the vertical offset is known, these values can be used in conjunction to trigonometrically resolve three important parameters, uplift, dip slip, and contraction. The trigonometry used for the calculation of these components is included in Appendix C.

4. Results

4.1 Cosmogenic Ages of Millard Canyon Surfaces

4.1.1 Qf4 Depth Profile

A total of five depth profile samples were measured for ^{10}Be concentrations with AMS methods. Sample 1303-1DP was run but produced no AMS current and it was abandoned after several attempts to activate the target with the Cesium plasma beam. Samples 1303-2DP, 1303-3DP, 1303-4DP and 1303-5DP all produced method-acceptable currents (average 10.5mA, range 3-17mA; See appendix B). Sample $^{10}\text{Be} / ^9\text{Be}$ ratios were corrected for Boron by LLNL. Sample background levels were corrected by the process blank *1303-Blank*. Our lab blank for these samples produced a $^{10}\text{Be}/^9\text{Be}$ ratio of 9×10^{-15} . Ratios were then converted to ^{10}Be concentrations in atoms per gram of quartz and are shown plotted in Figure 4.1 with 1σ error bars. Plotted versus depth ($\pm 5\text{cm}$), these concentrations fit an exponential decay curve (Figure 4.1) indicating approximately 10,000 atoms basin-wide inheritance, similar to the values determined from active channel ^{10}Be samples (McGuire, 2011). The surface age based on the depth profile was determined with linear regression using EXCEL “linest” function (DeVecchio et al., 2012). In this method, the slopes of the regression can be used to calculate the age; the age of the material is theoretically equal to the slope “m” of a line, divided by local production rate (Figure 4.2). Age errors are equivalent to the errors of the regression. The slope of the least squares fit line is 54201 ± 6820 . Assuming a production rate of 6.97 atoms/gram/year (calculated in the CRONUS calculator), this method yields an age range of 7776 ± 979 (2σ error) years for Qf4.

4.1.2 Surface Boulders

Surface exposure samples obtained from Qf4 were analyzed for ^{10}Be concentrations by AMS. Sample 1303-5 ran poorly and produced negligible currents (See appendix B). Samples 1303-1, 1303-2, 1303-3 and 1303-4 produced AMS currents at method-acceptable levels [average 6.5 mA, range 3-17 mA]. Sample ^{10}Be to ^9Be ratios were corrected for Boron at LLNL and background levels corrected by the process blank *1303-Blank*. Ratios were

then converted to ^{10}Be concentrations in atoms g^{-1} and are shown in Figure 4.3 with 1σ error bars. Processing of sample parameters through the CRONUS online calculator provides 1σ internal and external errors. Analysis of age data using smoothed probability density function Matlab script (Balco, 2008), shows the variance in data reduction approaches between the Balco Camel Plot and mean weighted averages determined using Isoplot (Figure 4.4). The two humps displayed in the camel plot graphically identify sample 1303-B2 as an outlier according to Balcos methodology. I find the mean weighted average age using all four boulder samples and this is plotted within the camel plot for comparison. Finding the weighted mean age of the 1303 boulder samples using the *internal* error yields an age of 6285 ± 330 with 2σ error.

4.1.3 Preferred Age of Qf4

By performing statistical evaluation of the Qf4 data including surface boulders and depth profile, a preferred age for the alluvial surface is determined. To compare the boulder exposure dates with the depth profile age, the *external* error of the boulder ages must be used instead of the *internal* error as is used when comparing samples within a group, as is described in Balco (2008). The mean weighted age of the four boulder samples and the depth profile, calculated using Isoplot 4 is 6800 ± 550 yrs (2σ).

4.2 Burial Samples- Qh Heights Fanglomerate

Five samples were processed for extraction of ^{10}Be and ^{26}Al . Sample 1301-4 was lost due to problems identified during sample preparation and so was not sent to LLNL for AMS analysis. (See discussion section for detail of observations). Reduction of the burial sample data yielded four burial ages, two of which are methodologically unfeasible. Samples 1301-1 and 1301-2 returned negative burial ages (-1.76 Ma and -1.27 Ma) based on their respective $^{26}\text{Al}/^{10}\text{Be}$ ratios of 15.46 and 12.27. This high ratio validates the assumption that perhaps some of the samples did not fully undergo complete quartz separation, as these ratios above 6.75 imply "extra" Aluminum that could not have been "produced" by cosmogenic processes. Samples 1301-3 and 1301-5 however provided ratios indicating non-negative ages. Sample 1301-3 returned a burial age of $680 \text{ ka} \pm 250 \text{ ka}$ with a $^{26}\text{Al}/^{10}\text{Be}$ ratio of 4.89. Sample 1301-5 returned a burial age of $1300 \text{ ka} \pm 260 \text{ ka}$, with a $^{26}\text{Al}/^{10}\text{Be}$ ratio of 3.67.

Consideration of these two results provides a best-estimate for age maximum of the Qh surface at 680-1300 ka. All four samples run returned consistent ^{10}Be ratios with reasonable 1σ uncertainties (see appendix B), again suggesting the problems are the result of feldspar-derived Aluminum.

4.3.1 Scarp Heights, Components and Rates- Southern Fault Area F2

Qf4 Scarp

Faulting is observed to offset Quaternary Alluvial unit Qf4 across the north 25° dipping San Gorgonio Pass Thrust as it passes through Millard Canyon (Figure 2.5). The scarp offsetting Qf4 has a measurable vertical offset of 12.7 ± 1.4 m (Figure 4.5a). Trigonometric resolution of the observed vertical component of displacement along the 25° dipping fault plane yields a dip slip component of 30 ± 3.3 m. Further resolution yields a contractional (horizontal) component of 27.2 ± 3.0 m (Table 4.1).

Using the constrained age of surface stabilization of Qf4 (6800 ± 550 ybp), this resolves into a set of kinematic rates normal to the fault plane strike. The calculated uplift rate on F2 is 1.86 ± 0.3 mm yr^{-1} . The calculated dip slip rate is 4.4 ± 0.6 mm yr^{-1} . The calculated horizontal contraction rate is 4.0 ± 0.5 mm yr^{-1} (Table 4.1).

Qf1 Scarp

Faulting is observed to offset Quaternary Alluvial unit Qf1 across the north 25° dipping San Gorgonio Pass Thrust as it passes through Millard Canyon (Figure 2.5). The scarp offsetting Qf1 has a measurable vertical offset of 1.9 ± 0.2 m (Figure 4.5b). Trigonometric resolution of the observed vertical component of displacement along the 25° dipping fault plane yields a dip slip component of 4.5 ± 0.5 m. Further resolution yields a contractional (horizontal) component of 4.1 ± 0.4 m (Table 4.1). Due to incomplete age constraints on surface Qf1, it was not used to calculate rates.

4.3.2 Scarp Heights, Components and Rates- Northern Fault Area F1

Qf3 Scarp

Faulting is observed to offset Quaternary Alluvial unit Qf3 across the north 45° dipping reactivated Banning Strand as it passes through Millard Canyon (Figure 2.5) The scarp offsetting Qf2 has a measurable vertical offset of 3.1 ± 0.7 m (Figure 4.5c). Trigonometric resolution of the observed vertical component of displacement along the 45° dipping fault plane yields a dip slip component of 4.4 ± 1.0 m. Further resolution yields a contractional (horizontal) component of 3.1 ± 0.7 m (Table 4.1). Due to large uncertainty in the age constraints available for Qf3, it was not used to calculate rates.

Qf2 Scarp

Faulting is observed to offset Quaternary Alluvial unit Qf2 across the north 45° dipping reactivated Banning Strand as it passes through Millard Canyon (Figure 2.5) The scarp offsetting Qf2 has a measurable vertical offset of 1.8 ± 0.1 m (Figure 4.5d). Trigonometric resolution of the observed vertical component of displacement along the 45° dipping fault plane yields a dip slip component of 2.5 ± 0.1 m. Further resolution yields a contractional (horizontal) component of 1.8 ± 0.1 m (Table 4.1).

Using the constrained age of surface stabilization of Qf2 (1270 ± 80 ybp), this resolves into a set of kinematic rates normal to the fault plane strike. The calculated vertical uplift rate on F1(Qf2) is 1.4 ± 0.1 mm yr⁻¹. The calculated dip slip rate is 2.0 ± 0.1 mm yr⁻¹. The calculated horizontal contraction rate is 1.4 ± 0.1 mm yr⁻¹ (Table 4.1). See Figure 2.6 for a latitudinal cross section of the terraces with age data.

5.0 Discussion

5.1 Inflation and Deflation of Alluvial Surfaces

The occurrence of surface *inflation* and *deflation* both have direct implications on the interpretation of in situ cosmogenic dating approaches. In this study, I rely on the exposure ages to represent the age of surface stabilization, and so any surface modification due to erosion, deposition or mass wasting subsequent to deposition of surface boulders will directly complicate the interpretation process. As the cosmogenic age data I have obtained serves as the basis for the interpretations, a thorough evaluation is made to identify any indications of surface modification.

5.1.1 Evidence of Surface Modification- Qf4 Surface Exposure Samples

Inflation of the ground surface subsequent to surface stabilization will effectively bury a target surface boulder and decrease the overall cumulative cosmic ray dosage of that sample by shading the direct exposure of incident cosmogenic ray bombardment. This will theoretically slow down the in-situ production rate of ^{10}Be within the quartz fraction of the sample, thereby making the exposure age younger than actual. Surface *deflation* of the alluvium underlying a surface exposure boulder will not directly affect the sample; deflation will not expose the boulder sample to any greater amount of incident rays; although it may maximize the exposure. If, however surface deflation induces surface *destabilization* and minor to major translation of surface material occurs, as may occur on an alluvial fan, significant difficulties will be introduced into the interpretation of ages. For example, if a group of surface boulders become rotated or reworked they may become oriented in a non-uniform way complicating subsequent interpretations. If reworking of surface material proximal to the study area occurred, this may introduce foreign material to this group, including boulders of varying exposure histories. Subsequent attempts at dating this surface with cosmogenic exposure samples will yield an age incorrectly representing the exposure history of the area targeted by the investigator. The relatively similar age ranges and statistical grouping of the surface exposure samples run for ^{10}Be in this study indicate no major evidence of surface destabilization. Sample 1303-B2 yielded an age that varied slightly from the group as observed in the statistical camel plot (Figure 4.3), however the variance is not significant enough to indicate major surface reworking. The transport history of these boulder samples is interpreted to be the result of a singular high energy event, causing rapid transport through the canyon arroyo. This rapid transport theoretically bypasses expected residence time of a particle in the active channel thereby cosmogenic

dose inheritance is minimal to “non-existent” for these samples. As previously discussed, cosmogenic inheritance is the result of CRN exposure during transport and residence time in a wash. This is validated by the difference in concentration of the boulders and the projected concentration of the depth profile curve for Qf4 (Figure 4.1). The difference is coincidentally equivalent to the ~10,000 atoms/gram of quartz inheritance observed in this study and McGuire (2011). After a review and evaluation of the observable evidence of surface modification in the record, I consider the ages of the individual, as well as the statistical variance of the group to indicate the Qf4 surface is undisturbed and the boulder exposure results are acceptable.

5.1.2 Evidence of Surface Modification - Depth Profile

Depth profile suites rely on internal relationships of depth and CRN concentration between the samples to serve their function (as described in methods section). Surface *inflation* of depth profiles may insulate the profile from maximum cosmogenic nuclide production, resulting in a younger age. Surface deflation of a depth profile suite requires the ablation of the surface through either eolian or hydrologic processes. These processes tend to remove finer-grained particles including silts and very fine sands, thereby physically fractionating the alluvium, which increases the fraction of coarser grained siliciclastic material. This removal of interstitial material effectively lowers the bulk density of the alluvium, which directly affects the attenuation of incident rays and promotes deeper penetration of radiation into the subsurface. Modification of this depth parameter theoretically alters the idealized decay profile, which obfuscates and complicates the interpretation of the depth profile behavior.

The depth profile obtained from the Qf4 surface in this study showed no observable indications of surface inflation or deflation. The “ideal” decay plot matches well with that observed from the Qf4 pit, and this is strengthened by the interpreted ^{10}Be inheritance values of ~10k atoms/g. This value, which was independently derived using the depth profile method in this study is congruent with that determined by McGuire for the Millard Canyon drainage (McGuire, 2011). This similarity in inheritance values between two distinct methodologies (this study and that of McGuire) provides a very good foundation on which to validate the soundness of the linear regression age results from this depth profile. The depth profile derived age data and inheritance values are also complimentary to the ages provided by the surface exposure samples. The averaging of the values from the boulder exposure samples and the depth profile regression using a mean weighted average is the preferred statistical method when combining values with variable error ranges (Leo, 1994).

5.1.3 Burial Sample AMS Results – Qh Ages

Of the four samples submitted for AMS, all had method-acceptable ^{10}Be currents and resultant ratios (Appendix B). The AMS currents and resultant ratios for ^{26}Al were not as robust however, likely due to processing failures pre-AMS analysis. Inherent difficulties isolating the aluminum are likely the cause of sample corruption. The initial step of quartz separation is intended to remove all mineral phases that are not pure SiO_2 . If the mineral separation procedure is not completed, the sample material will be contaminated with feldspar-derived isotopes of Aluminum. Problems experienced with sample 1301-4 were likely due to incomplete quartz separation as well as resultant faulty ion-exchange column steps. The 1301-4 sample corruption was validated with three approaches before it was abandoned. The first indication of problems with the sample was high concentration of Al in the partial sample aliquot (PSA), nearly 10 times greater than that observed of other samples. Second, an unusual milky appearance was observed after the cation exchange step; the sample maintained milky appearance through the anion exchange as well, which for this particular sample was slower than other samples. Samples (1301-1, 1301-2, 1301-3, and 1301-5) were eluted through columns at relatively rapid rates, while sample 1301-4 had observably fewer elution drips per second. This, the third line of evidence is interpreted to be the result of high levels of feldspar contamination resulting from incomplete quartz separation steps.

5.1.4 Scarp Height Measurement - Qf4 Surface Continuity Across F2

Imagery analysis of Millard Canyon shows variability in the density of creosote bush *Larrea tridentata* across the F2 footwall surfaces (Figure 5.1). Specifically, a higher density of smaller colonies in the area mapped by Yule and Sieh (2003) as Qf1 compared to those areas mapped at Qf4. Creosote bush are observed to begin colonization of surfaces in arid environments with closely spaced groups. Over time, colony maturity is characterized by larger colonies more spaced apart due to extensive root networks (up to 10' radius) competing for water resources. This effect is the result of the asexual cloning the plant uses to survive times of drought (Marshall, 1995). This asexual cloning yields large circular bush colonies around the root crown similar to that observed on the Qf4 surface. On newly stabilized surfaces such as within the Millard Canyon active channel and Qf1 surface of Yule and Sieh (2003), the development of creosote is dependent on seed abundance and water. This can be observed in the active channels of Millard Canyon with tightly spaced creosote colonies, where the ephemeral surface water availability promotes active germination of new seeds allowing for new growth. Shallow roots are able to tap into

the shallow groundwater within the active channel. Colonies on the Qf4 surface however have been presumably uplifted farther above the water table and so have had to expand their root systems as far lateral as is possible. Surface Qf4 above F2 maintains a population of creosote colonies, which is very similar in spacing and size to the colonies distal to the fault scarp. I interpret this to provide strong indication that the Qf4 surface is continuous above and below the scarp where the LiDAR cross sections were mensurated. The stark difference in bush spacing and size across the units mapped by Yule and Sieh (2003) as Qf4 and Qf1 provides a method to relatively date the surfaces by vegetation development. One caveat is that anthropogenic activities on the fan surface to include farming, pipelines, and drilling have modified the *Larrea Tridentada* population and so this application must be used with discretion. A second caveat is that average lifespan for a plant is ~1200 years, however in nearby Johnson Valley, CA the largest clone is observed to be > 9000 years old. Nonetheless, I interpret the qualitative similarity of the *Larrea Tridentada* bushes proximal and distal to the fault to indicate that the Qf4 surface is undisturbed.

5.2 Estimation of Coseismic Deformation

I use the deformation components measured in scarp profiles to analyze and propose the likelihood of possible paleoseismic scenarios. Using the age constraints provided by the newly dated Qf4 surface and the trigonometrically calculated dip slip values presented in section 4, I bracket the accumulated dip slip over the “lifespan” of the stabilized surface. This provides the opportunity to assess the cumulative slip on faults F1 and F2 of this study. Using the datasets available, the slip per event can be estimated by evaluating the cumulative slip on the youngest scarps on faults F1/F2 and interpreting the likely number of seismic events that have led to their present state of development (Method A), or by multiplying the long-term slip rate by the interpreted recurrence interval (Method B). Paleoseismic data collected and deciphered by McBurnett (2011) yields an estimated recurrence interval (RI) of 630 years for structures in Millard Canyon. I use this frequency component estimate as a multiplier in Method B to evaluate and discuss the slip recorded in scarps within Millard Canyon. One caveat to both approaches is that I assume a standard time-predictable recurrence interval to evaluate these scenarios. Additionally, the respective faults (F1/F2) have differing proportions of strike slip to dip slip which are complex, related to subsurface fault orientations, and not entirely understood. To effectively communicate and discuss the surface features I will aim to refer to surface offset at faults as the name of the surface with a forward slash to identify the fault which bisects it for example “Qf3/F1” is referring to surface Qf3 at Fault 1.

5.2.1 Banning Strand SAF - F1

5.2.1.1 F1 Dip Slip per Event

Recorded within surface Qf2/F1 is a total of 2.5 ± 0.1 m of dip slip. This cumulative slip is constrained temporally within the age range of the Qf2 material at 1270 ± 80 ybp (McBurnett, 2011). I make the relatively safe assumption the penultimate event (EII) at ~ 1200 ybp was responsible for driving the uplift of the Qf2 and the later occurrence of the most recent event (EI) ~ 600 ybp would have then caused further growth on the Qf2 scarp. Assuming the two events EI and EII cumulatively represent the current observable dip slip of 2.5 ± 0.1 m within Qf2, I mathematically deduce (Method A) these seismic events each produced $\sim 1.3 \pm 0.1$ m of dip slip per event on fault F1.

Following the alternate (Method B) approach, I multiply the calculated fault-specific long term dip slip rate in mm/yr presented in section 4.3 by the recurrence interval interpreted by McBurnett (2011) of 630 years. This method yields per event dip slip values of 1.3 ± 0.1 m.

5.2.1.2 F1 Net Slip per Event

These dip slip values estimated in Section 5.2.1.1 are a minimum as they only represent the dip slip component of motion. Yule and Sieh (2003) observed an approximate Holocene strike slip to dip slip ratio of 1.8:1 on F2. If applying the mean weighted average dip slip per event value from above (1.3 ± 0.1 m), this would mean a concurrent strike slip per event rate for the fault F1 of 2.3 ± 0.2 meters per event. This will sum with the dip slip component into a net slip vector of $\sim 2.8 \pm 0.3$ meters per event. Alternatively, resolving the dip slip into net slip using the formulas of Thompson et al (2002) yields a net slip per event value on fault F1 of 1.8 ± 0.1 meters per event. As the observation of Yule and Sieh (2003) represent actual site behaviors and empirical strike slip to dip slip proportions, a preference is given to the values obtained using these calculations. The key finding however is that both approaches yield an average net slip per event of ~ 2 meters on fault F1 (Banning Strand).

5.2.2 - San Gorgonio Pass Fault - F2

5.2.2.1 F2 Dip Slip per Event - *Undefined Recurrence Interval*

The scarp at Qf1/F2 represents cumulative dip slip component of 4.5 ± 0.5 m resulting from either one or two cumulative seismic events (McBurnett, 2011). The presence of this scarp is not useful for direct calculation of long term slip rates as it is not clear whether it has completed a full recurrence cycle, it is however useful to interpret potential per-event kinematics. If the Qf1/F2 scarp has undergone only one seismic event (EI), then a total 4.5 ± 0.5 m of coseismic uplift occurs on F2 per event. To perform a circular check on this, a propagation of this per-event rate “into” the measured cumulative uplift of Qf4 yields an estimate of 7 ± 1 EQ’s which is indicative of a RI of 970 ± 160 years which is a lower frequency than that determined by McBurnett (2011). Alternatively, if the Qf1/F2 surface has undergone two events (EI, EII), dip slip would be approximately 2.3 ± 0.3 m / event. This rate, integrated back “into” the Qf4 scarp height would require twice the number of seismic events (13 ± 2) to yield the amount of cumulative vertical displacement measured on the F2/Qf4 scarp. This higher frequency of $\sim 520 \pm 90$ year R.I. is closer to that concluded by McBurnett (2011).

5.2.2.2 F2 Dip Slip Per Event - *Defined Recurrence Interval*

By multiplying the long-term rates derived from Qf4 presented in section 4.3.2 by the recurrence Interval (RI) of McBurnett (2011) of 630 years using quadratics, I obtain a dip slip per event value of 2.8 ± 0.4 m. This number and those from section 5.2.2.1 are all similar in theme; they all show 2 meters or more of dip slip per event on an active thrust fault (F2).

6.0 Conclusion

6.1 Conclusion - Slip Transfer Through SGP

A primary objective of this study is to determine the contribution of the faults in the SGP to the regional slip transfer of the San Andreas Plate Boundary Transform Fault. Studying dated and deformed alluvium such as that found in Millard Canyon can provide insight into the in-situ local fault plane slip behavior. Understanding how this local fault plane slip geometrically interacts with the fault strands entering and leaving the SGP allows for the determination of the amount of San Andreas plate boundary transform slip this deformation represents.

Complex sub-surface orientation of the SGPF makes it difficult to understand how the slip measured in Millard Canyon is transferred to faults exiting SGP. Analysis of the surface traces of the faults shows the thrust fronts of the complex tear faults in SGP to have an approximate azimuth of $\sim 240^\circ$, nearly 70° oblique from the transform plate boundary motion (Figure 6.1, 1.4). This study observed no evidence of strike slip motion on the San Gorgonio Pass Thrust, (F2) and so the slip motion is most likely transferred by mechanism(s) other than how it would be on a continuous fault plane. A simplified interpretation of this geometry is presented in Figure 6.2, showing how deformation on a contractional step over such as is interpreted in SGP can be translated into transform strike slip motion on a regional fault segment. This very simplified geometry shows that the component of contraction is 1:1 with the strike slip on the parent fault segment entering and exiting the stepover. What this geometry potentially shows is that horizontal contraction is an indication of crustal Peninsular Range-Type basement (Matti, 2014) moving with respect to the adjacent San Gabriel Mountain Type basement. This slip, coincidentally striking N45W (314°) vector, still only represents a portion of the total SAF transform plate boundary slip, as the SAF slip is also partitioned to other fault zones such as the San Jacinto faults and ECSZ. This geometry is based on a 90° angle between the incoming/outgoing segments, the lateral ramps, and the thrust frontal ramps which is not observed in SGP. Of note was the azimuth of the lateral ramps connecting the frontal ramps of 317° , strikingly similar to the 314° of the SAF in the Coachella/Salton Trough and the northern sections (Figure 1.4). If these lateral ramps are accommodating the contractional components as shown in Figure 6.2, the strike-slip azimuth is equivalent to the main transform boundary fault.

6.2 Conclusion – SGP Fault Team

“Large Active Oblique Reverse Fault seeking Low angle thrust fault to help accommodate increasing contractional strain in the San Gorgonio Pass...work may be part time or on an as-needed basis” -Banning Strand SAF

The interpreted values of both long term and per event dip slip on F2 (southern fault) are over twice that of F1(northern fault). Lower dip angles on F2 likely promote lower coefficients of friction allowing for accommodation of more dip-slip on the F2 fault plane. This is prudent with the theory of recent (125kyr) onset of displacement on F2, perhaps to accommodate a new tectonic stress regime in which SAF fault motion is suddenly redirected through SGP, applying immense crustal strain to the ancestral Banning Fault. Prior to onset of this recent (125kyr) strain regime, the Banning Strand served as a multi-talented “workhorse” for SGP, accommodating both strike slip components as well as contractional components that were transferred through SGP (as oblique reverse slip). I interpret that fault F2 propagated out of necessity to help distribute some of the new contractional component of the SAF system through the SGP. The pair of faults in this study seem to work together as an efficient team to accommodate large magnitude crustal strain rates at this plate boundary interface. The primary role of the Banning Strand, the longtime SGP veteran is to accommodate the majority of strain as the oblique reverse components. The role of the relatively juvenile San Gorgonio Pass Thrust is to accept any additional contractional strain that occurs in the step over.

If viewing the San Gorgonio Pass fault as a “helper” fault whose job it is to deal with the “overflow” contraction that the Banning Strand cannot accommodate, it is very plausible that the recurrence behavior on this series of faults is not a simple time-predictable model, and perhaps the two faults do not rupture contemporaneously, instead with variation in the recurrences. An example of this might manifest as earthquakes on the Banning Strand every 600 years, with slip on the SGPT every 800 years. Or perhaps the behavior of the faults in SGP is still even more complex with variations in the timing and rhythm (polyrhythmic), where activity begins and ceases producing earthquake “swarms”. For simplicity sake, interpretations in this study were made using a basic time-predictable model of recurrence (as reliable as a metronome). Further beneficial work might include increasing the resolution of the paleoseismic record through continued trenching activities within SGP. Also, advancements in dating methods of surfaces may help to place sharper constraints on surface ages and thereby provide more detailed long-term slip

rates. Had the burial dating efforts attempted in this study provided useful burial ages for the Qh- Heights Fanglomerate, a late Pleistocene slip rate for the Banning Strand would have helped to shed more light on the development of the active structures studied in Millard Canyon and SGP.

6.3 Conclusion – Potential For Large Magnitude Events

A consistent finding throughout this study was identification of per event slip averages of ~2 meters on each of the faults in SGP. By applying both the empirical observations of Yule and Sieh (2003) and trigonometric methods of Thompson (2002), the data of F1 shows a minimum oblique net slip value of ~2 meters per event. The San Geronio Pass Thrust, for which no evidence of strike slip motion was observed, returned per event dip slip motion of at minimum ~2, but up to ~4 meters. These observations are the evidence that interseismic strain is accumulating in the southern extent of the San Andreas fault system and being released into SGP on a recurring yet infrequent basis. The resultant deformation is evidenced as a series of Holocene scarps and terrace risers which provide a decipherable record of the past seismic activity in SGP through the greater part of the Holocene. The question is not *does* SGP experience large magnitude infrequent earthquakes, but when will the next one be. Based on the summed slip components for both faults assuming a contemporaneous rupture, SGP may accommodate at minimum 4 meters or more of local fault plane slip. The M_w 7.3 Landers earthquake in 1992 for example had an average slip of 3-4 meters (<http://scedc.caltech.edu/significant/landers1992-rupture.html>). Due in part to the increased complexity of the fault network in SGP, and proximity to the crustal plate boundary it may be safe to assume a larger event perhaps on the order of magnitude of the M_w 7.8 Shakeout Scenario event.

A question still stands however; is the SAF capable of producing through-going ruptures in SGP? The initial and typical interpretation is that the presence of scarps = successful earthquakes are and have been occurring, along with the expected post seismic strain drop. An even more extreme scenario would be where seismic events outside of SGP are sending in slip, but due to structural complexities, SGP is not letting this out. If SGP has not been having through going ruptures, then these growth structures investigated in this study may be indications of interseismic strain accumulation at unfathomable levels. If this scenario were played out, this buildup of interseismic strain could have the potential of producing very large magnitude earthquakes. If SGP is capable of through going ruptures, then there is most certainly evidence of this large magnitude event out there somewhere, in some trench, terrace riser or scarp waiting to be found!

References

- Allen, C.R., 1957, San Andreas fault zone in the San Gorgonio Pass, southern California: Geological Society of America Bulletin, v. 68, p. 315–350.
- Atwater, Tanya, (1970), Implications of Plate Tectonics for the Cenozoic Tectonic Evolution of Western North America: Geological Society of America Bulletin, v. 81, p. 3513-3536.
- Balco, G., Rovey C.W. II, 2008. An isochron method for cosmogenic-nuclide dating of buried soils. American Journal of Science 308, pp. 1083-1114
- Balco, G., Stone, J., Lifton, N., and Dunai, T., 2008, A simple, internally consistent, and easily accessible means of calculating surface exposure ages and erosion rates from Be-10 and Al-26 measurements: Quaternary Geochronology, v. 3, p. 174–195, doi: 10.1016/j.quageo.2007.12.001.
- Carena, S., Suppe, J., and Kao, H., 2004, Lack of continuity of the San Andreas fault in southern California: Three dimensional fault models and earthquake scenarios: Journal of Geophysical Research, v. 109, no. B4, paper B04313, doi: 10.1029/2003JB002643.
- Cook, M. L., Dair, L.C, 2011 Simulating the recent evolution of the southern big bend of the San Andreas fault, Southern California. Journal of Geophysical Research, v. 116, B04405.
- DeVecchio, D. E., Heermance, R. V., Fuchs, M., 2012a, Climate-controlled landscape evolution in the western Transverse Ranges, California; insights from Quaternary geochronology of the Saugus Formation and strath terrace flights: Lithosphere, v. 4, p. 91-109.
- Gosse, J.C., Phillips, F.M., 2001. Terrestrial in situ cosmogenic nuclides: theory and application. Quat. Sci. Rev. 20, 1475–1560.
- Hough, Susan, 2010. Predicting the Unpredictable: The tumultuous science of earthquake prediction, Princeton University Press.

- Ivy-Ochs, Susan, Duhnforth, M., Densmore, A.L., Alfimov, V., M.L. Dating Fan Deposits with Cosmogenic Nuclides. Schneuwly-Bollschweiler et al. (eds.), *Dating Torrential Processes on Fans and Cones*, Advances in Global Change Research 47, DOI 10.1007/978-94-007-4336-6 16, © Springer Science+Business Media Dordrecht 2013.
- Jones, L., L. Hutton, D. Given, and C. Allen, The North Palm Springs, California, earthquake sequence of July 1986, *Bull. Seismol. Soc. Am.*, 76, 1830–1837, 1986.
- Lal, D., 1991. Cosmic ray labeling of erosion surfaces: In situ production rates and erosion models: *Earth and Planetary Science Letters*, v. 104, p. 424–439
- Langenheim, V.E., Jachens, R.C., Matti, J.C., Hauksson, E., Morton, D.M., and Christensen, A., 2005, Geophysical evidence for wedging in the San Gorgonio Pass structural knot, southern San Andreas fault zone, southern California: *Geological Society of America Bulletin*, v. 117; no. 11/12, p. 1554–1572.
- Leo, W. R. 1992, *Techniques for Nuclear and Particle Physics Experiments*, .. Springer-Verlag .
- Magistrale, H., and Sanders, C., 1996, Evidence from precise earthquake hypocenters for segmentation of the San Andreas Fault in San Gorgonio Pass: *Journal of Geophysical Research*, v. 101, p. 3031–3041, doi: 10.1029/95JB03447.
- Marshall, K. Anna. 1995. *Larrea tridentata*. In: *Fire Effects Information System*, [Online]. U.S. Department of Agriculture, Forest Service, Rocky Mountain Research Station, Fire Sciences Laboratory (Producer). Available: <http://www.fs.fed.us/database/feis/> [2017, October 1].
- Matti, J.C., Morton, D.M., and Cox, B.F., 1985, Distribution and geologic relations of fault systems in the vicinity of the central Transverse Ranges, southern California: U.S. Geological Survey Open-File Report 85-365, 23 p.
- Matti, J.C., and Morton, D.M., 1993, Paleogeographic evolution of the San Andreas fault in southern California: A reconstruction based on a new cross-fault correlation, in Powell, R.E., Weldon, R.E., II, and Matti, J.C., eds., *The San Andreas fault system: Displacement, palinspastic reconstruction, and geologic evolution*: Geological Society of America Memoir 178, p.107–159.
- McBurnett, P., 2011, Paleoseismicity of the San Gorgonio Pass Fault Zone at the Millard Canyon: Testing the likelihood of a through-going San Andreas rupture [M.S. thesis]: California State University Northridge.

- McGuire, K. E., 2011, Tracking Cosmogenic ^{10}Be in Multiple Grain Sizes Down and Alluvial System in an Active Orogen. [M.S. thesis]: California State University Northridge.
- Morton, D., J. Matti, and J. Tinsley, Banning fault, Cottonwood canyon, San Geronio pass, southern California, in Cordilleran Section of the Geological Society of America, edited by M. Hill, pp. 191–192, Geol. Soc. of Am., Boulder, Colo., 1987.
- Noble, L. F., The San Andreas rift in the desert region of southeastern California, Year Book Carnegie Inst. Washington, 31, 355–363, 1932.
- Oskin, M., Stock, J., and Martín-Barajas, A., 2001: Rapid localization of Pacific–North America plate motion in the Gulf of California, *Geology*, v, 29, no. 5 p. 459-462
- Oskin, M., and Stock, J., 2003: Pacific–North America plate motion and opening of the Upper Delfín basin, northern Gulf of California, Mexico, *Geological Society of America Bulletin*, v 115, p. 1173-1190
- Rasmussen, G., Reeder, W., 1986. What happens to the real San Andreas fault at Cotton wood canyon, San Geronio Pass, California?. *Geology Around the Margins of the Eastern San Bernardino Mountains*, Inland Geological Society, Redlands, California, pp.157-162.
- Rood, D.H., Burbank, D.W., Finkel, R.C., 2011, Spatiotemporal patterns of fault slip rates across the central Sierra Nevada Frontal Fault Zone, *Earth and Planetary Science Letters*, 301, 457-468, doi:10.1016/j.epsl.2010.11.006.
- Seeber, L., and Armbruster, J.G., 1995, The San Andreas fault system through the Transverse Ranges as illuminated by earthquakes: *Journal of Geophysical Research*, v. 100, no. B5, p.8285–8310.
- Sieh, K., and R. H. Jahns, Holocene activity of the San Andreas Fault at Wallace Creek, California, *Geol. Soc. Am. Bull.*, 95, 883–896, 1984.
- Sykes, L.R., and Seeber, L., 1985, Great earthquakes and great asperities, San Andreas fault, southern California: *Geology*, v. 13, p. 835–838.
- Spinler, J.C., Bennett, R.A., Anderson, M.L., McGill, S.F., Hreinsdóttir, S., and McCallister, A., 2010, Present-day strain accumulation and slip rates associated with southern San Andreas and Eastern California shear zone faults: *Journal of Geophysical Research*, v. 115, p. B11407, doi:10.1029/2010JB007424.

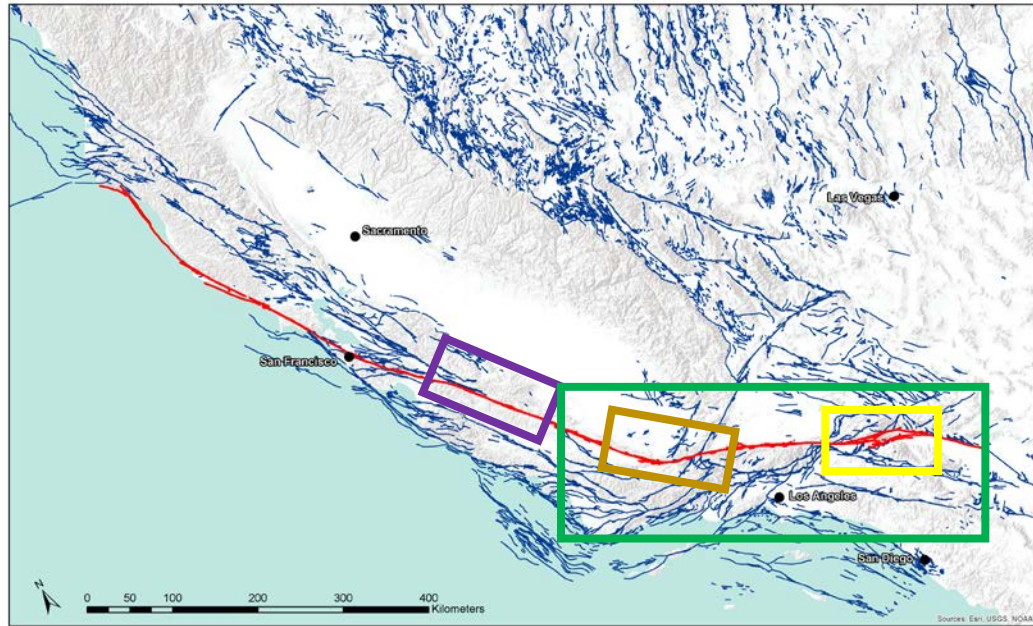
Spotila, J., Farley, K., Sieh, K., 1998. Uplift and erosion of the San Bernardino Mountains associated transpression along the San Andreas fault, California, as constrained by radiogenic helium thermochronology. *Tectonics*, Vol. 17, pp360-378.

Thompson, Steven C., Weldon, R.J., Rubin, C.M., Abdrakhmatov, K., Molnar, P., Berger, G.W., 2002. Late Quaternary slip rates across the central Tien Shan, Kyrgyzstan, central Asia *Journal of Geophysical Research*, VOL. 107, NO. B9, 2203, doi:10.1029/2001JB000596.

Weldon, R.J., II and Sieh, K. E., 1985, Holocene rate of slip and tentative recurrence interval for large earthquakes on the San Andreas fault, Cajon Pass, Southern California. *Geological Society of America Bulletin*, v 96, p. 793-812.

Yule, D., and Sieh, K., 2003, Complexities of the San Andreas fault near San Geronio Pass: Implications for large earthquakes: *Journal of Geophysical Research*, v. 108, no. B11, ETG 9-1-9-23.

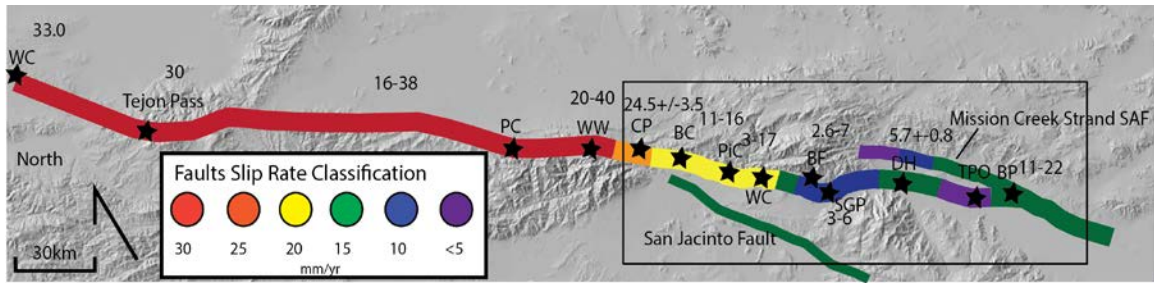
Figure 1.1



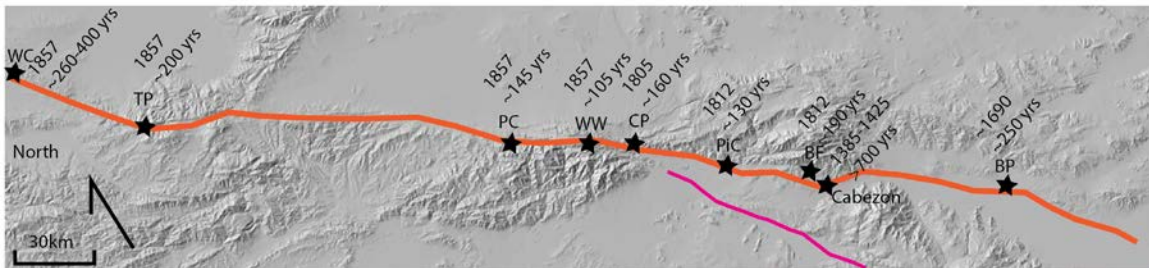
San Andreas Fault Zone (SAFZ) shown as heavy red line, from Salton Trough on the right, extending over 1200km up to Cape Mendocino at the far left. Blue line features are displaying USGS Quaternary Fault dataset. Transverse Range/Southern San Andreas Fault Zone in green extent. Big Bend/Tejon Pass area in orange extent. Creeping Segment in purple extent. San Geronio Pass Region in yellow extent. With major metropolitan areas shown in proximity.

Figure 1.2

A.

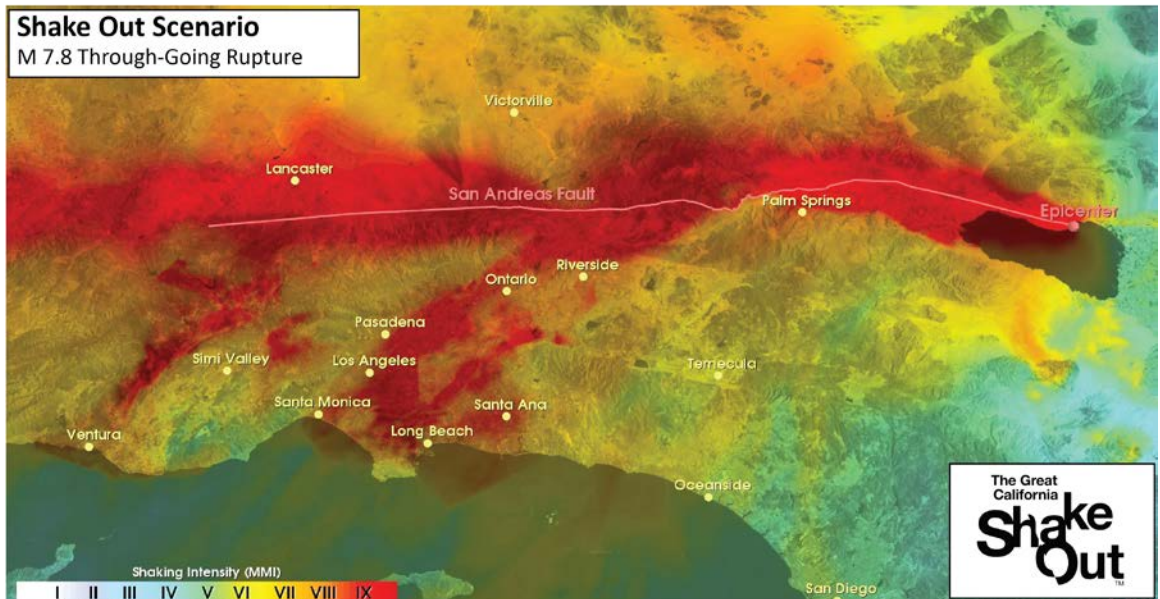


B.



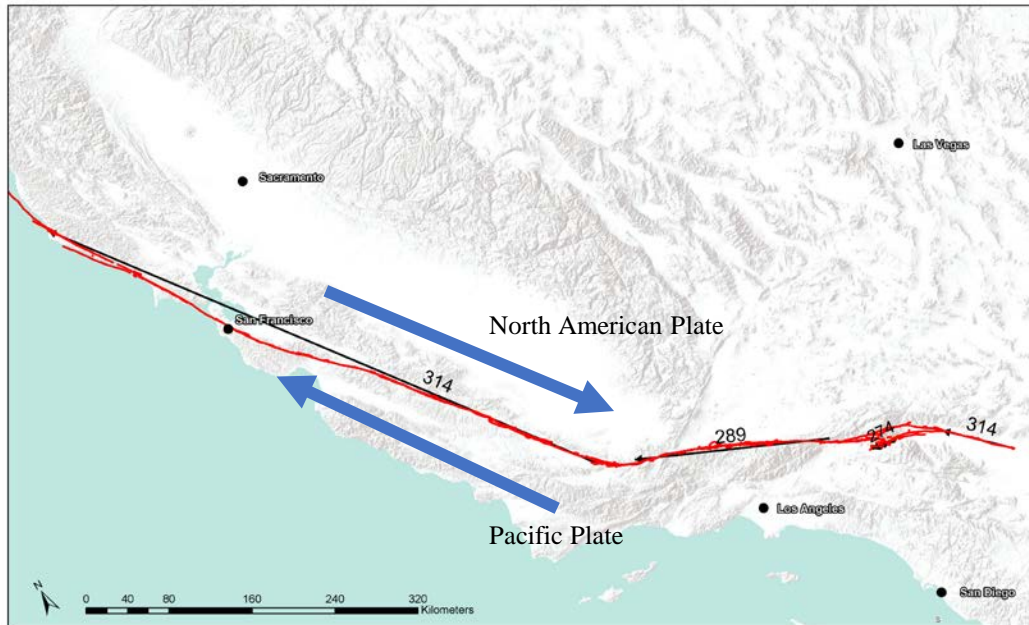
- A. Geologic slip rate gradient along SAF from Wallace Creek (WC) 33.9 ± 2.9 mm/yr; Tejon Pass (TP) 30 ± 6 mm/yr; Pallet Creek (PC) 35.6 ± 6.7 mm/yr; Wrightwood (WW) 20-40 mm/yr; Cajon Pass (CP) 24.5 ± 3.5 mm/yr; Badger Canyon (BC) $13 \pm 4 \pm 2$ mm/yr; Pitman Canyon (PiC) 19 mm/yr; Wilson Creek (WC) 14-25 mm/yr; Burro Flats (BF) 8 ± 4 mm/yr; San Gorgonio Pass (SGP) 5.7 ± 0.8 mm/yr; Devers Hill (DH) 7-15 mm/yr; Thousand Palms Oasis (TPO) 2-6 mm/yr; Biskra Palms (BP) 14-17 mm/yr; (Sieh and Jahns, 1984; Eberhard-Phillips et al., 1990; Salyards et al., 1992; Fumal et al. 1993; Weldon and Sieh, 1985; McGill et al., 2010; Harden and Matti, 1989; Orozco and Yule, 2003; McBurnett, 2011; Fumal et al. 2002a; Behr et al., 2010).
- B. Paleoseismic data for San Andreas Fault including date of most recent large magnitude earthquake and recurrence interval. Wallace Creek (WC) (Sieh and Jans 1984), Tejon Pass (TP) (Sykes and Seeber 1985), Pallet Creek (PC) (Sieh et al., 1989), Wrightwood (WW) (Fumal et al., 1993), Cajon Pass (CP) (Weldon and Sieh, 1985), Pitman Canyon (PiC) (McGill et al. 2010), Burro Flats (BF) (Orozco, 2004), Cabezón (Yule and Sieh, 2003; McBurnett 2011; Ramzan 2012), Biskra Palms (BP) (Behr et al. 2010).

Figure 1.3



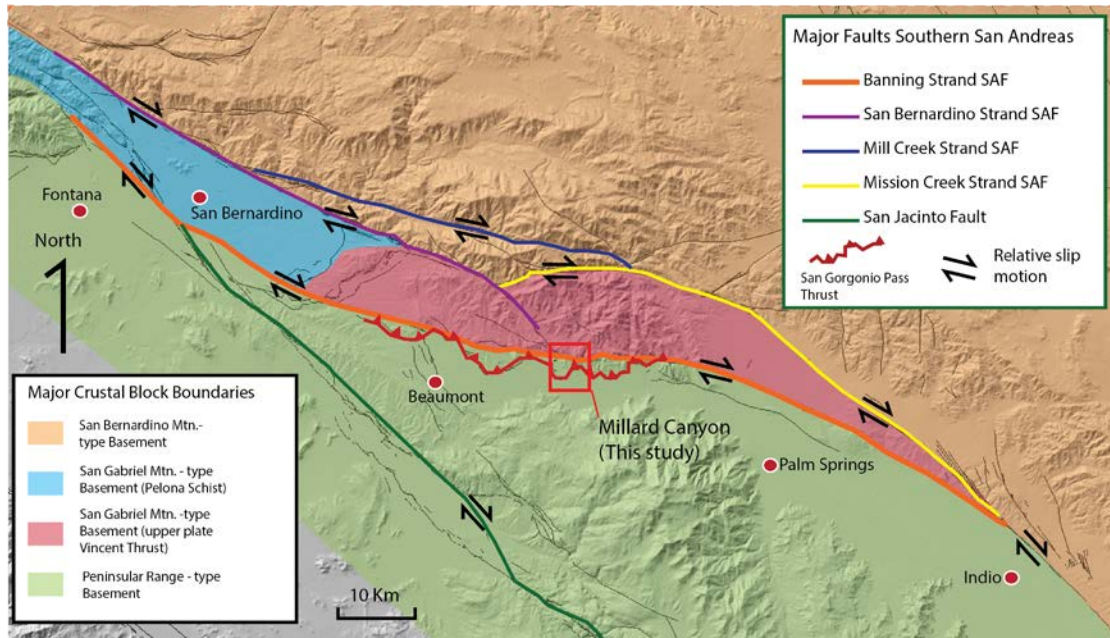
Modeled Ground Shaking Intensity of simulated M7.8 rupture on the Southern San Andreas Fault. Scenario depicts rupture originating at southern extent of SAFZ in the Salton Trough and advancing NW along SAF trace through the San Gorgonio Pass (SGP) left stepping structural knot. The released energy exceeds the shear strength of the SGP complexity and continues through the Mojave Section SAF (MSSAF). Intense ground shaking is shown to perpetuate through the LA Basin and along the San Cayetano Fault towards Ventura CA. LA Metropolitan population of 20+ million inhabitants will be exposed to high intensity ground shaking (in red). (SCEC.org)

Figure 1.4



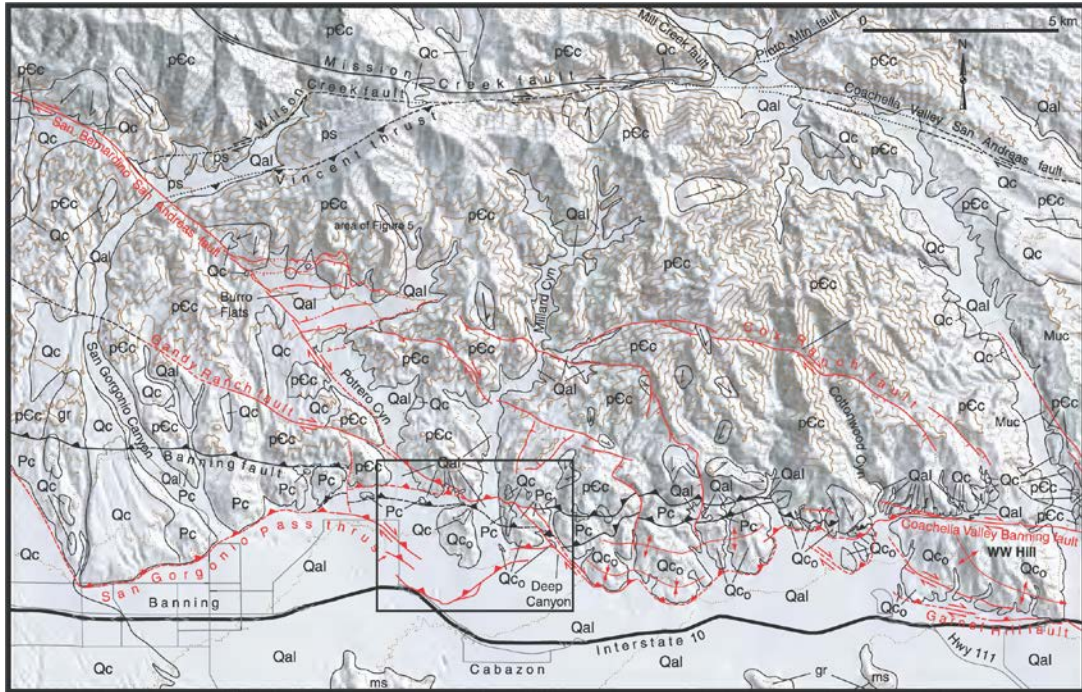
Variations in Azimuth along strike of North American/Pacific plate boundary transform fault (numbers shown in degrees). Note transition from 314° in Salton Trough to oblique azimuths through SGP and Mojave sections. Abrupt return to 314° azimuth, NW of the Big Bend suggests this is primary vector of sigma-1 strain. Blue arrows indicate relative plate direction. Azimuth calculated on WGS 84 Spheroid using Mean Line Azimuth geoprocessing tool in ArcGIS 10.3.

Figure 2.1



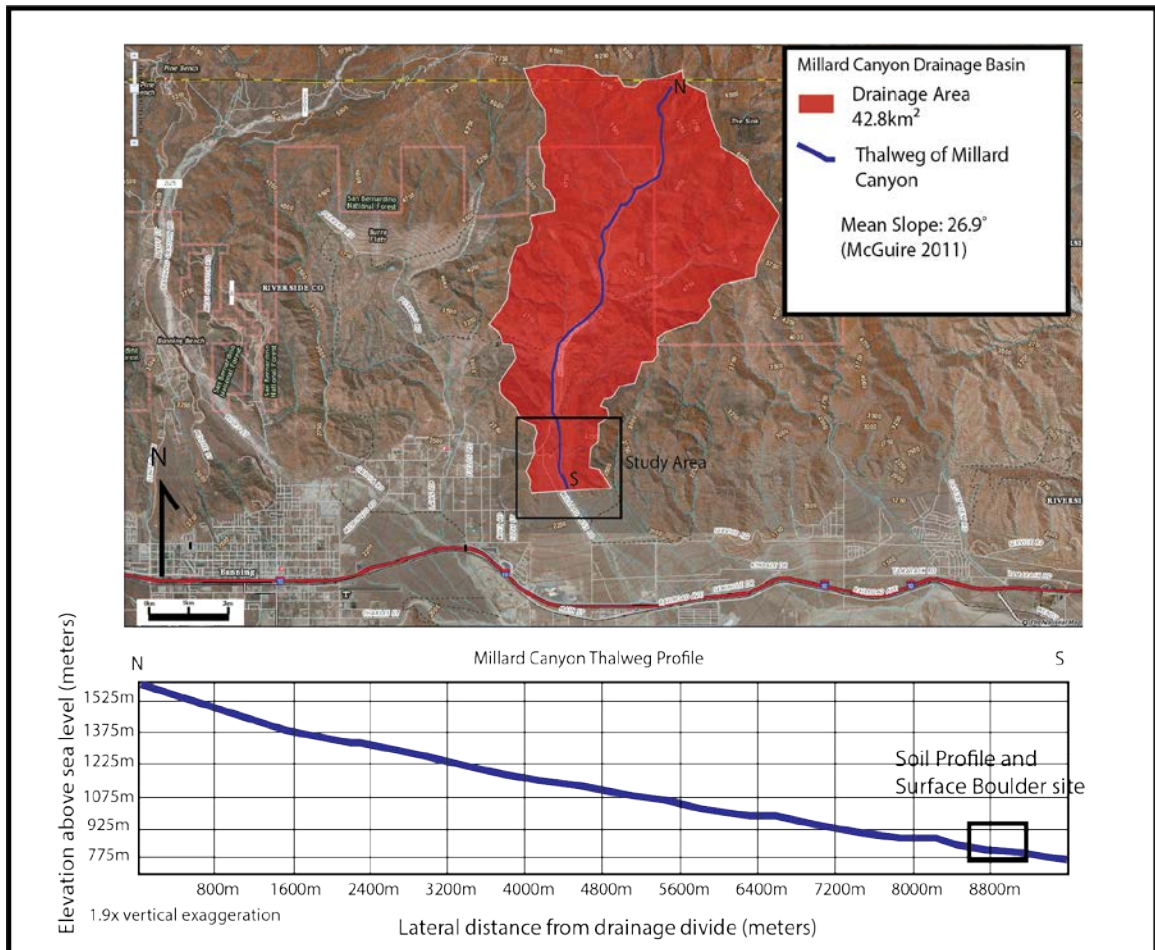
Major Crustal Blocks described by Matti (1985), contributing to complex fault geometries and strain regimes throughout the Southern San Andreas Fault Zone. Banning Strand SAF considered by Langenheim et al. (2005) to be crustal boundary separating North American Plate (NAP) and Pacific Plate (PP). San Gabriel Mountain type basement terranes are remnants of upper and lower plates of Vincent Thrust. Millard Canyon Study area located in red box at center of figure, along San Gorgonio Pass Thrust (SGPT) Layer overlay on 30m US Shuttle Radar Topography Mission (SRTM) DEM. (Modified from Matti (2014) and Langenheim et al (2005)).

Figure 2.2



Geologic map showing complex geometric fault traces through the of San Geronio Pass region from Yule and Sieh (2003). Inset box shows location of figure 16. Active faults represented by red trace, inactive faults in black. Observe trend of Banning Strand from west to east through Millard Canyon (inset box) with increasing complexity as it approaches Whitewater Hill. Trace of San Geronio Pass thrust follows toe of raised topography from Banning Bench to Cottonwood Canyon.

Figure 2.3



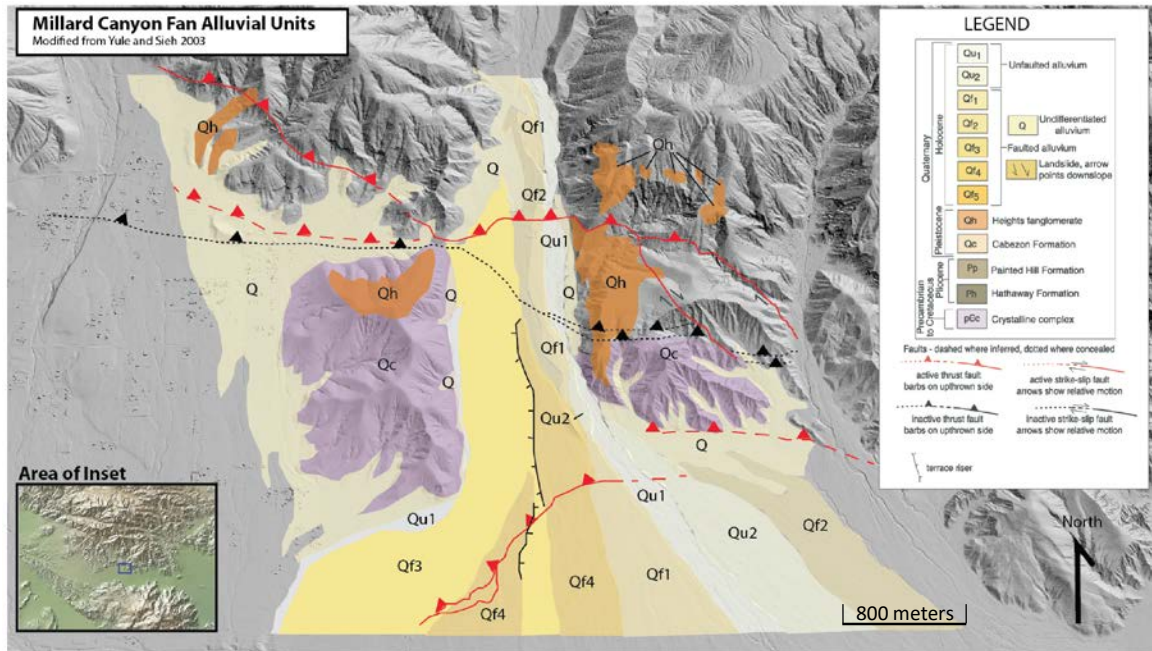
Plan view of Millard Canyon Drainage catchment extent in red polygon. Area calculated using USGS National Map Viewer GIS server. Thalweg topographic profile created in Google Earth Pro, overlain onto USGS TNM 2.0 Topo with Imagery.

Figure 2.4



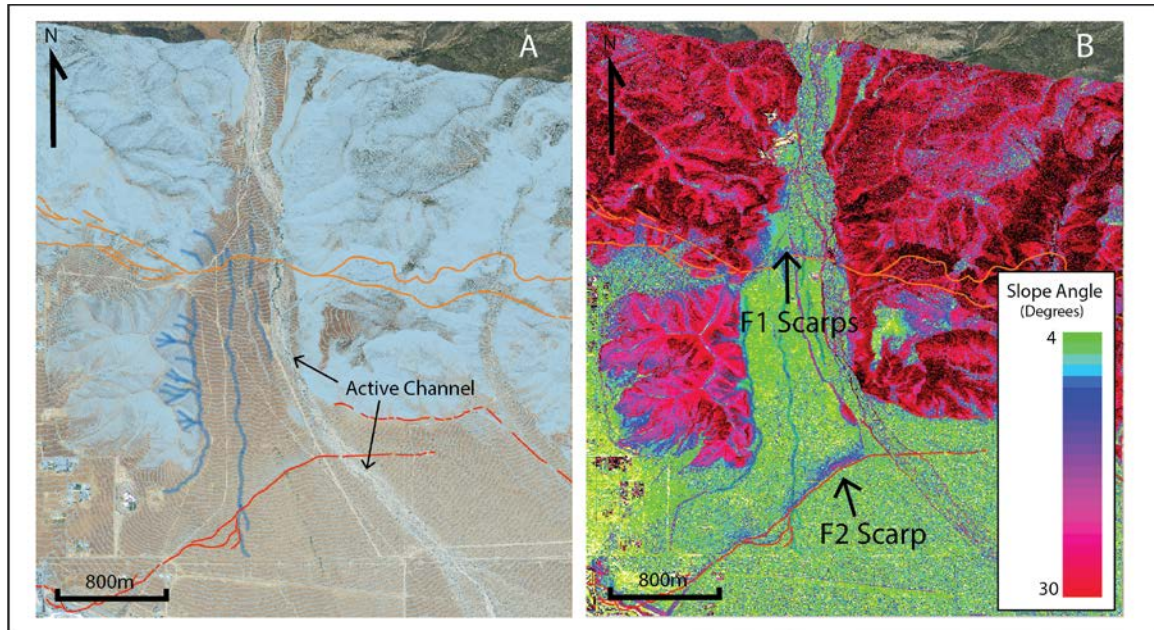
Drainage map of the San Gorgonio Pass region with 10m contour lines derived from SRTM 1/3 Arc Second elevation data. Contours extracted with GDAL v.1.2.29 in QGIS Brighton v.2.6. Black lines indicate general hydrologic flow of major drainage basins of the San Gorgonio Pass from west to east: San Gorgonio River (HUC 12-181002010102), Millard Canyon (HUC12-181002010104), and Whitewater Canyon Drainage (HUC12-181002010301). Variations in drainage base level due to tectonic driven uplift and or climate variability throughout the Holocene directly control sediment transport and throughput of the drainages. During wetter times, Millard Canyon would likely have been capable of discharging substantial volumes of sediment via hydrologic entrainment. Trends toward more arid climates in southern California during the Holocene (Bull,1991) have likely hastened mass transport of material from all but the the largest drainage area (Whitewater and San Gorgonio River basins). This trend is interpreted by the steeper contoured fan of Millard Canyon as it dumps into Cabazon. Faults are color-coded as follows: Orange: San Andreas Fault Zone, Red: San Gorgonio Pass Thrust, Blue: Pinto Mountain Fault, Magenta: San Jacinto Fault Zone.

Figure 2.5



Tectonic geologic map of Millard Canyon showing alluvial fan units as mapped by Yule and Sieh (2003). Un-faulted alluvium (Qu1, Qu2) within active channel. Older alluvium records slip events as preserved scarps, and are the focus of this study.

Figure 2.6



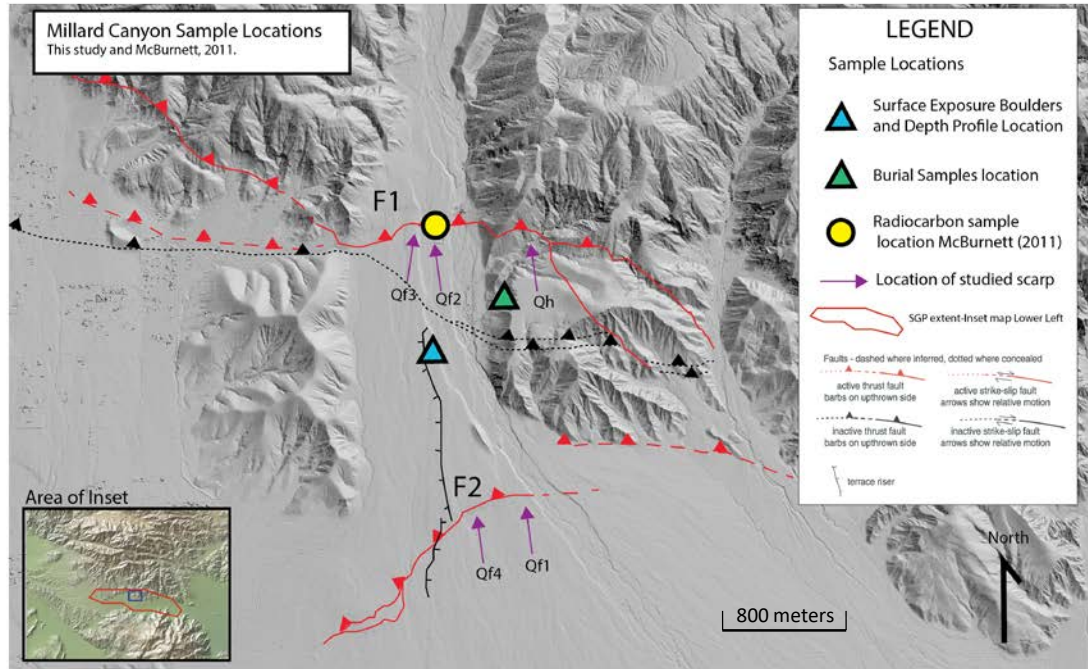
A. High resolution 0.5m contour interval map derived from B4 LiDAR dataset, extracted with GDAL v.1.2.29 using QGIS Brighton v.2.6. Surface runoff rivulets traced in blue are mapped using contours and USGS orthorectified aerial imagery. Northeastern most rivulet is a result of well pump test discharge during groundwater production well installation. Fault F1 in orange, fault F2 in red. **B.** High resolution slope map derived from B4 LiDAR dataset, generated using GRASS 6.4.3 raster processing module. Warmer colors represent steeper slope and is used to delineate scarp fronts from base level surfaces, and to determine ideal cross section locations.

Table 2.1

Reference	Segment / Site	Recurrence Interval	Geologic Slip Rate (mm/yr)	Geodetic slip rate (mm/yr)
San Bernardino Segment				
McGill et al. (2007)	Badger Canyon		14 +/- 3	
Harden and Matti (1989)	Yucaipa		14-25	
Weldon and Sieh	Cajon Pass		24 +/- 3.5	
Becker et al. (2005)	GPS			-2.0 +/- 15
Meade and Hager (2005)	GPS			5.1 +/- 1.5
Bennet et al. (1996)	GPS			26 +/- 2
Coachella Valley Segment				
Fumal et al. (2002)	Thousand Palms Oasis		4 +/- 2	
Behr et al. (2010)	Biskra Palms Oasis		12-21.7 (14-17 preferred)	
Van der Woerd et al. (2006)	Biskra Palms Oasis		15.9 +/- 3.4	
Dorsey (2003)			15 +/- 3	
Keller et al. (1982)	Biskra Palms Oasis		10-35	
Bennet et al. (2008)	GPS			6.7 - 10.7
Fay and Humphreys (2005)	GPS			22.3 +/- 0.7
Meade and Hager (2005)	GPS			23.3 +/- 0.5
Becker et al. (2005)	GPS			23.0 +/- 8
Bennet et al. (1996)	GPS			22 +/- 2
Banning Strand/San Gorgonio Pass				
Orozco (2004)	Burro Flats		2.6-7.0	
Yule et al. (2001)	Garnet Hill		5.7 +/- 0.8	
Matti et al. (1992a)	Millard Canyon		1-1.3 (partial uplift)	
Yule and Sieh (2003)	San Gorgonio Pass		5 (partial uplift)	
McBurnett (2011)	Millard Canyon	471-540	3.0-6	
Ramzan (2012)	Lion Canyon	600-700		
Yule and Sieh (2001)	Burro Flats	300		
Behr et al. (In press)	East Whitewater Hill		7-15	
sSAF transfer to ECSZ				
Meade and Hager (2005)	Eureka Peak Fault		21.3 +/- 1.6	
Entire sSAF				
Lindsey and Fialko (2012)	GPS			19.2 +/- 0.9 (dipping)
Fialko et al. (2005)	INSAR			25 +/- 3

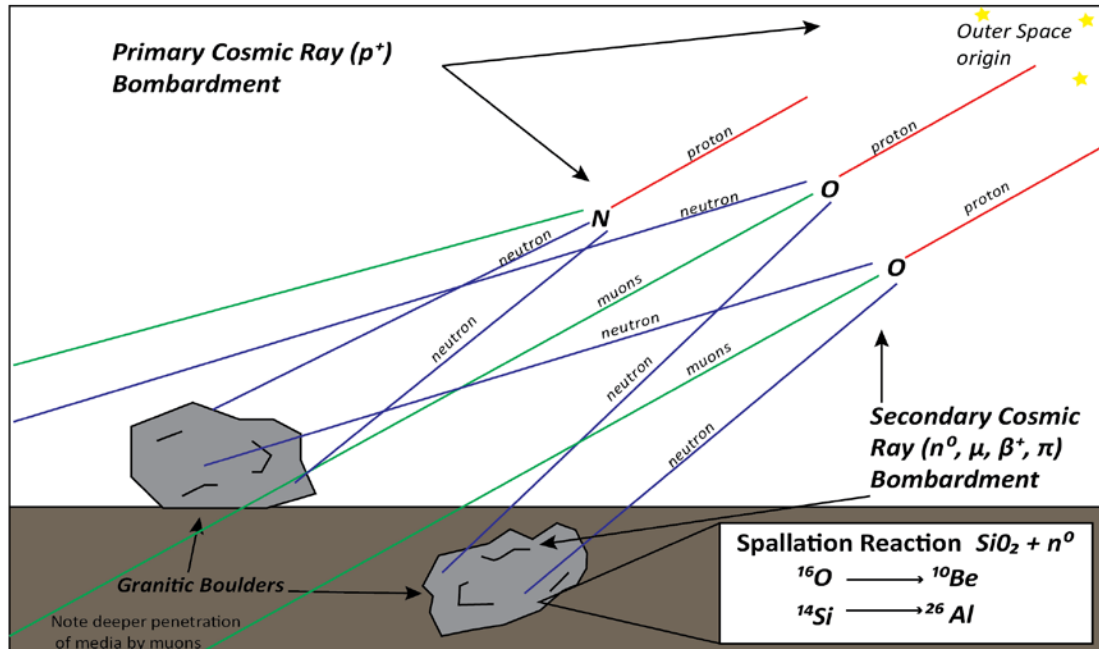
Compilation of slip rates for Southern San Andreas Fault segments. Data includes list of geologically-derived slip rates and available geodetically-derived slip rates. Select sites include recurrence interval data when available.

Figure 3.1



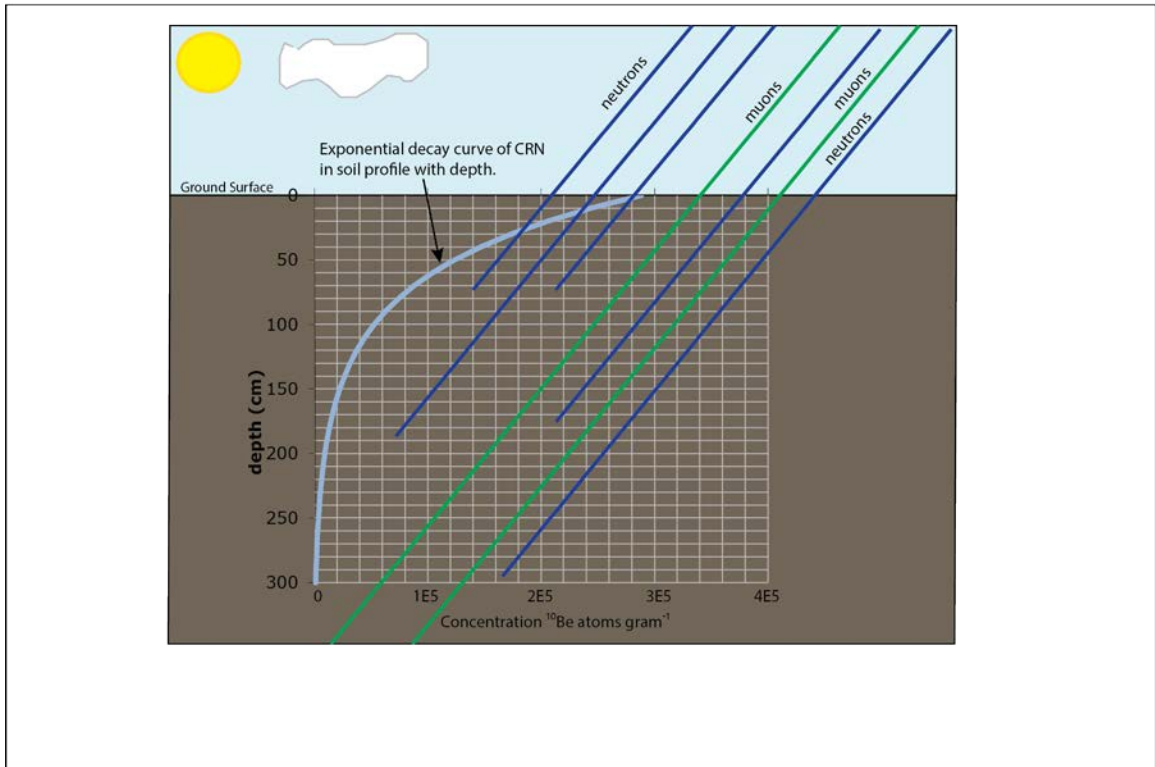
DEM of Millard Canyon study area, showing location of samples from this study and from McBurnett (2011). Scarp localities F1 and F2 shown on upper and lower active faults. This study measures heights of scarps indicated by purple arrows, labeled with the alluvial surface it offsets.

Figure 3.2



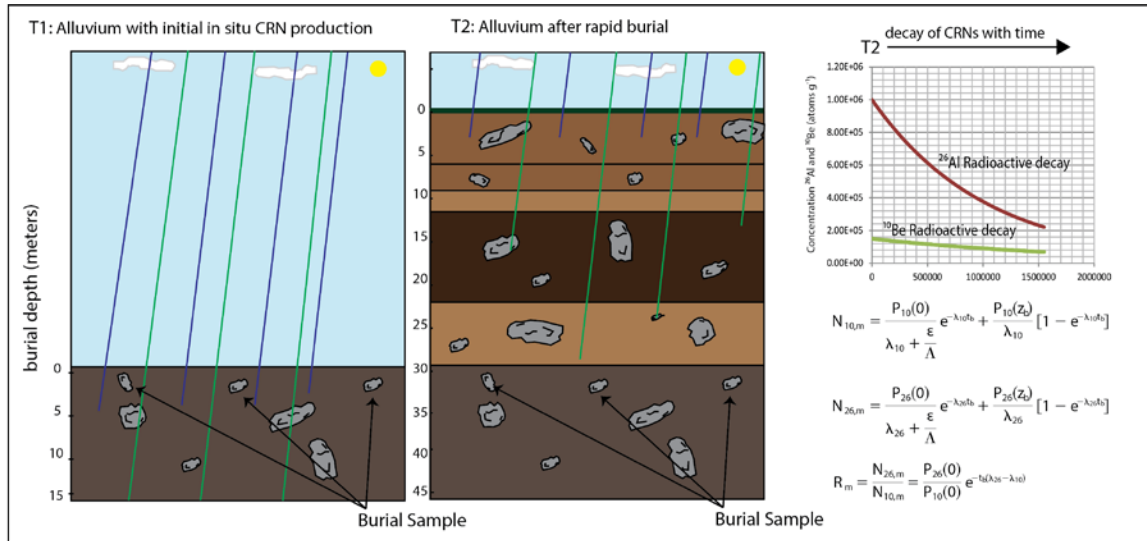
Formation of in-situ Cosmogenic Radionuclides (CRN) by spallation reactions. Primary cosmogenic rays originate in outer space from many sources including supernovae. Nucleons (primarily protons) bombard atmospheric gases such as Nitrogen (N) and Oxygen(O), releasing secondary cosmic rays as neutrons (n^0), muons (μ), positron(β^+) and pions (π). Neutrons and muons which play the largest role in CRN production, advance towards the earth surface impacting quartz (SiO_2) containing materials such as granite and siliciclastic alluvium (Lal, 1991). The impact causes spallation fission reactions to occur forming ^{10}Be and ^{26}Al isotopes from ^{16}O and ^{14}Si respectively. Neutron penetration diminishes with depth, with total attenuation at depths greater than $\sim 3\text{m}$ (Gosse, 2012). Muons may penetrate much deeper than neutrons especially in low density rock media such as alluvium, and can effectively form CRNs up to depths of 30m at very low production rates.

Figure 3.3



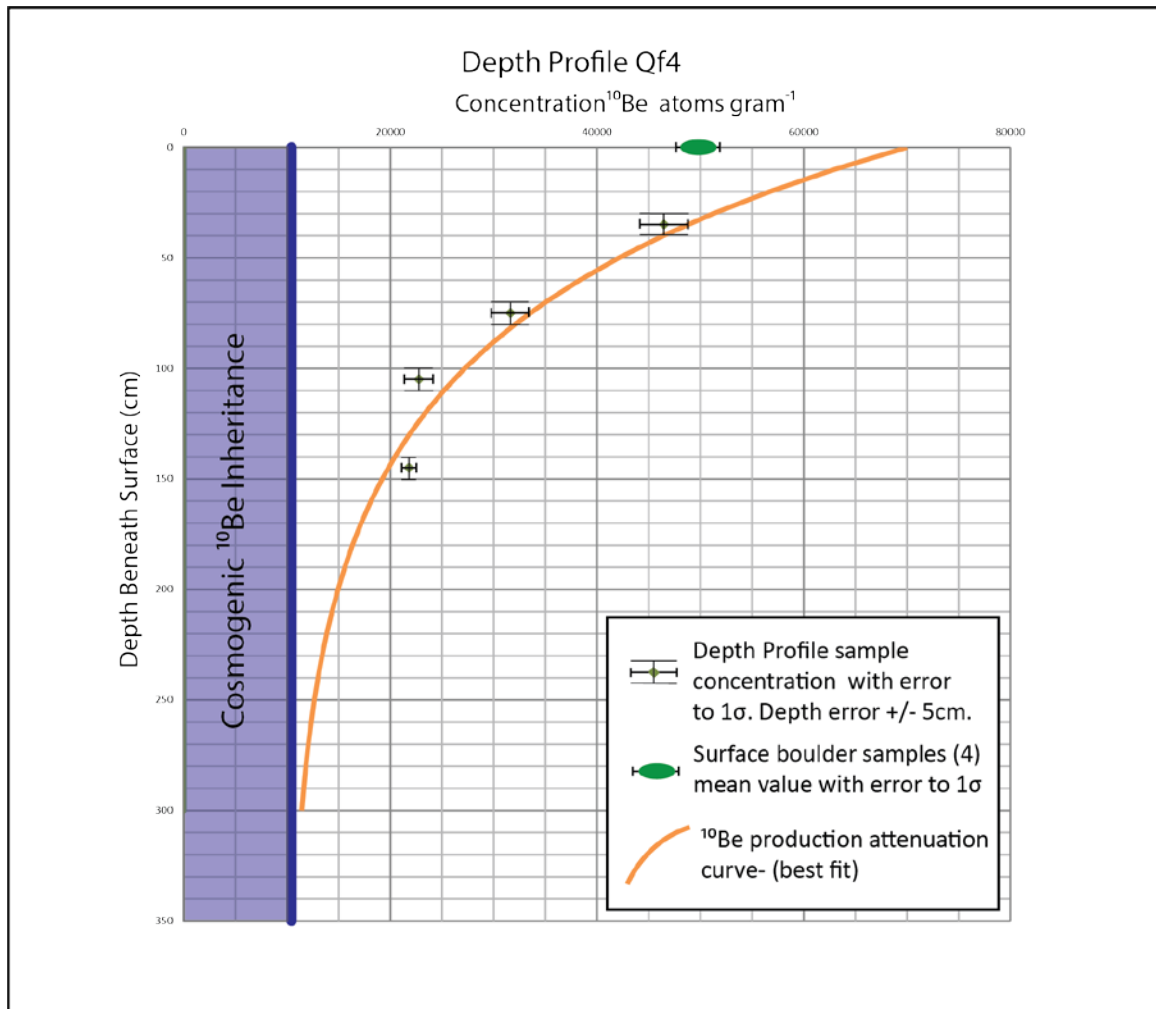
Depth Profile Concept. Incoming neutrons (blue) and muons (green) penetrate through the soil column causing spallation reactions to occur at depth. Neutrons can penetrate to depths of ~3m beneath surface; muons may penetrate down to 30m beneath surface. Attenuation of neutron penetration causes exponential decrease in production rate of CRN. This characteristic is the theoretical basis of depth profile method to determine CRN inheritance values. This figure shows soil with zero inheritance; CRN concentration curve approaches zero at roughly 3m depth.

Figure 3.4



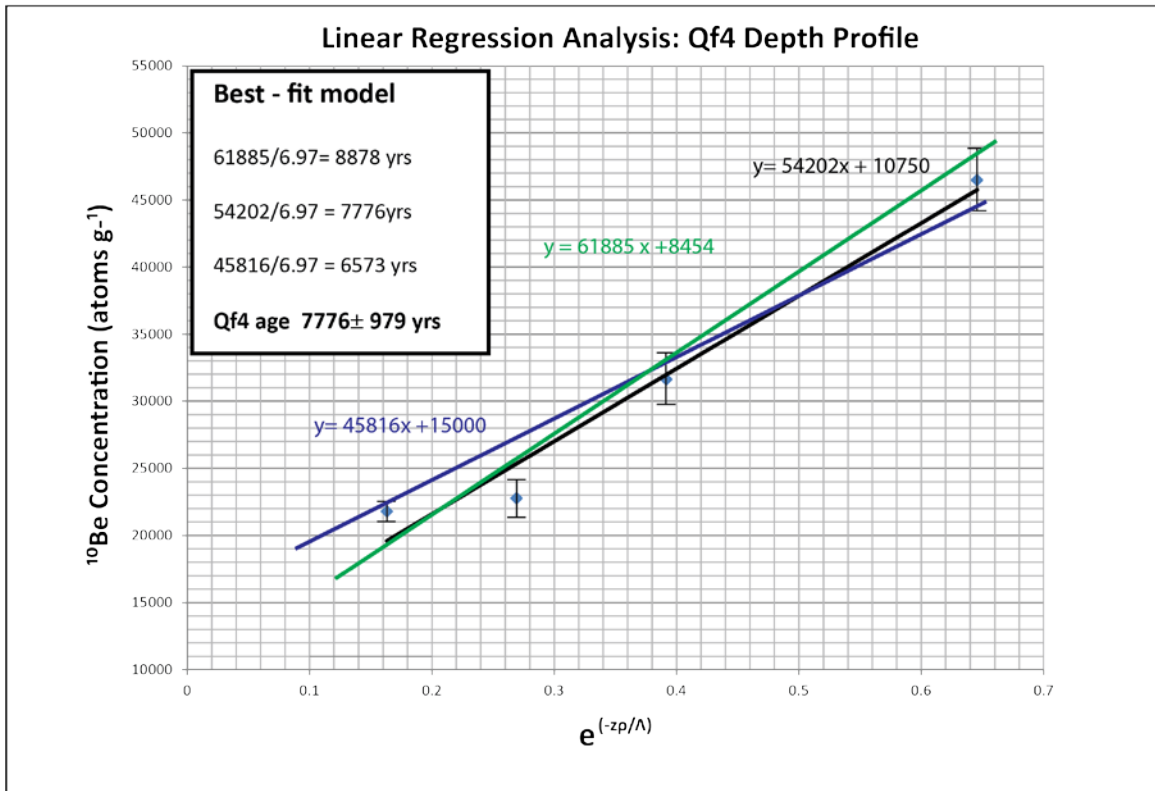
Theory of cosmogenic burial dating method. At time T1, alluvium is exposed to cosmic ray particles, neutrons (blue), and muons (green). Silica bearing rocks and sediments accumulate cosmogenic radionuclides ^{10}Be and ^{26}Al according to in-situ production rates via spallation reactions. These targets will accumulate over six times the amount of ^{26}Al isotope than ^{10}Be due to a higher isotopic production rate. At time T2, alluvial material is buried rapidly by mass transport event terminating production of CRNs below depths of 30m. With time the CRNs radioactively decay at their respective half-lives ($1.387\text{E}6$ and $7.17\text{E}5$ for ^{10}Be and ^{26}Al respectively). Upper right shows schematic decay plots of subject CRNs over the course of $1.5\text{E}6$ years. Burial dating relies on the ratio between CRNs using formulas in lower right. See Balco and Rovey (2008) for detailed discussion.

Figure 4.1



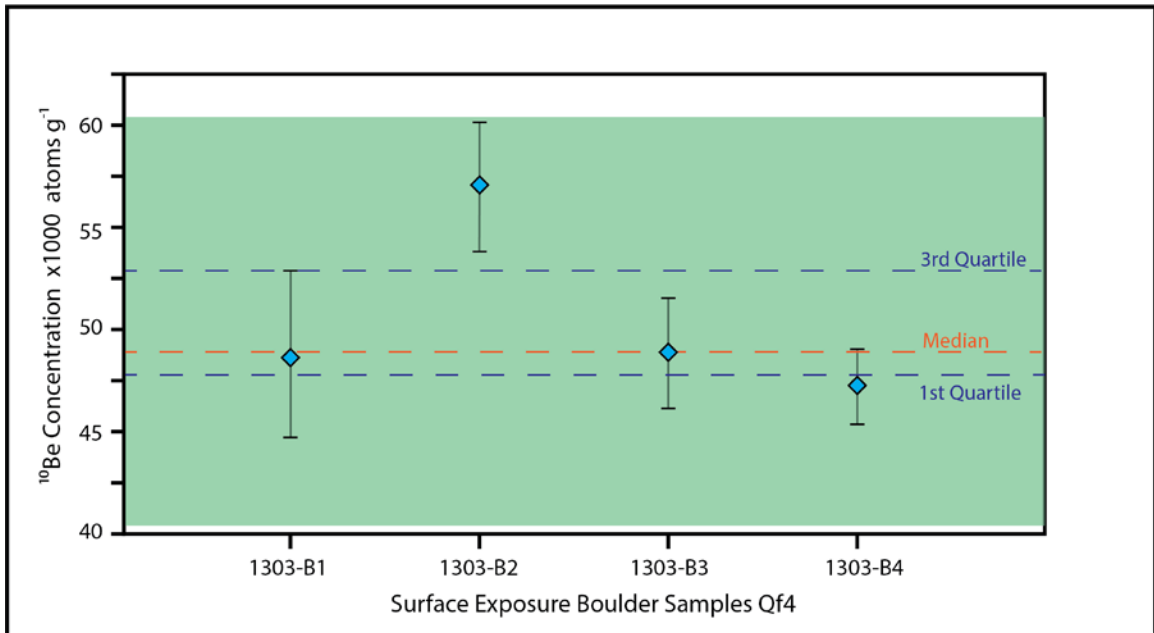
Depth profile curve- Qf4 alluvium of Millard Canyon, San Gorgonio Pass. Samples plotted with CRN production attenuation at depth decay curve. Effective production rate drops exponentially with depth due to attenuation of gamma radiation. Effect of muogenic radiation on CRN ages is negligible for late Quaternary/Holocene alluvium. Sample ^{10}Be concentrations plotted with 1-sigma error. Sample depth plotted with 5 cm error.

Figure 4.2



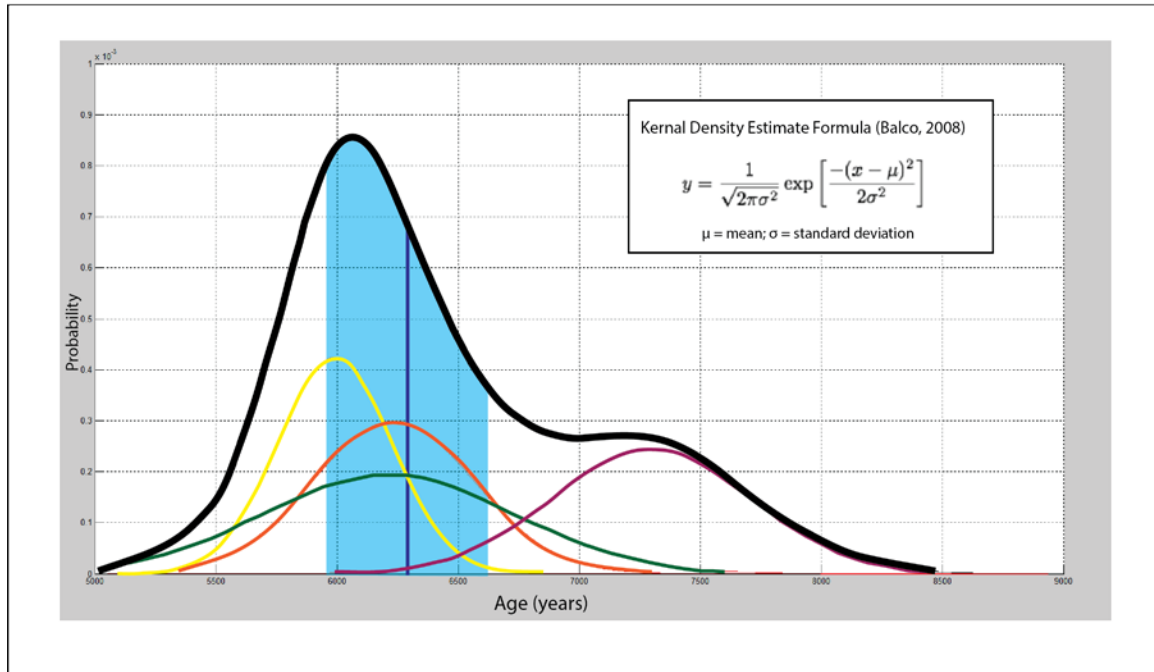
Linear regression analysis of Qf4 depth profile samples. Lines represent linear fits of concentration values within 1σ . Green line shows steepest plausible slope within error providing the age maximum. Purple line shows shallowest slope within error, providing age minimum. The median of these two ages is used as the base age assuming local production rate of 6.97 atoms/gram/year (Balco et al., 2008). Preferred age of Qf4 in Millard Canyon 7725 ± 1153 years.

Figure 4.3



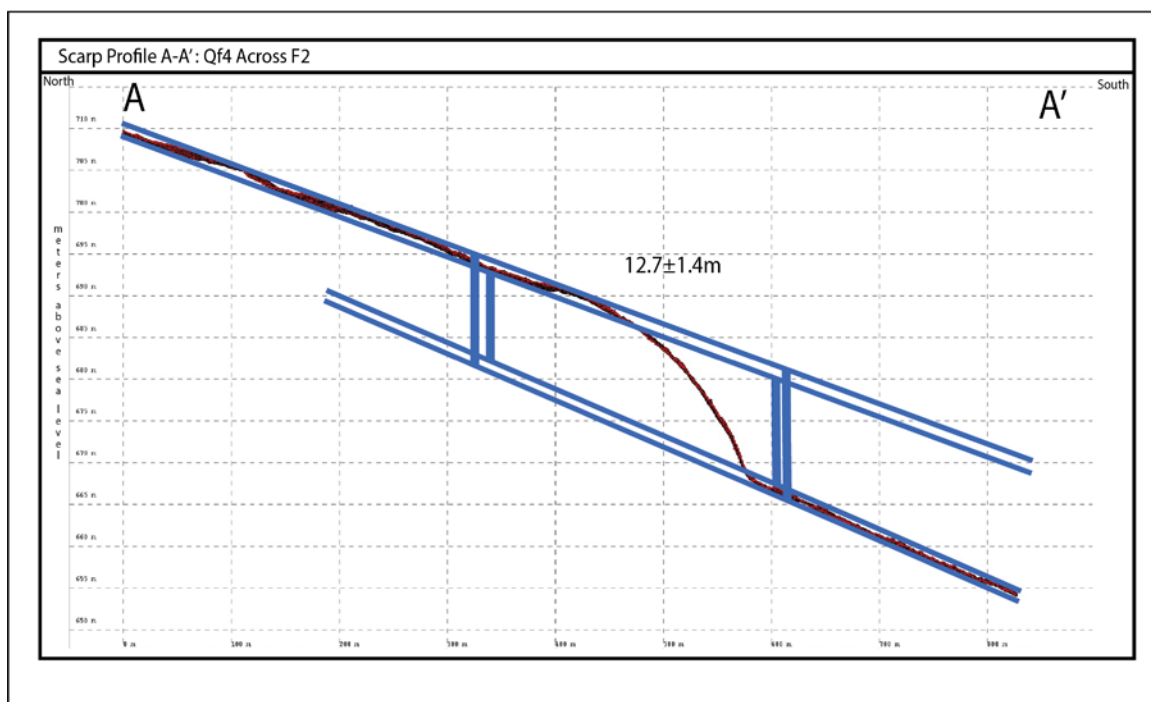
Surface exposure boulder sample ^{10}Be concentrations with 1σ error, assuming no erosion at surface and zero inheritance. Sage shaded box shows acceptable calculated data range, outside of which data is considered outlier.

Figure 4.4



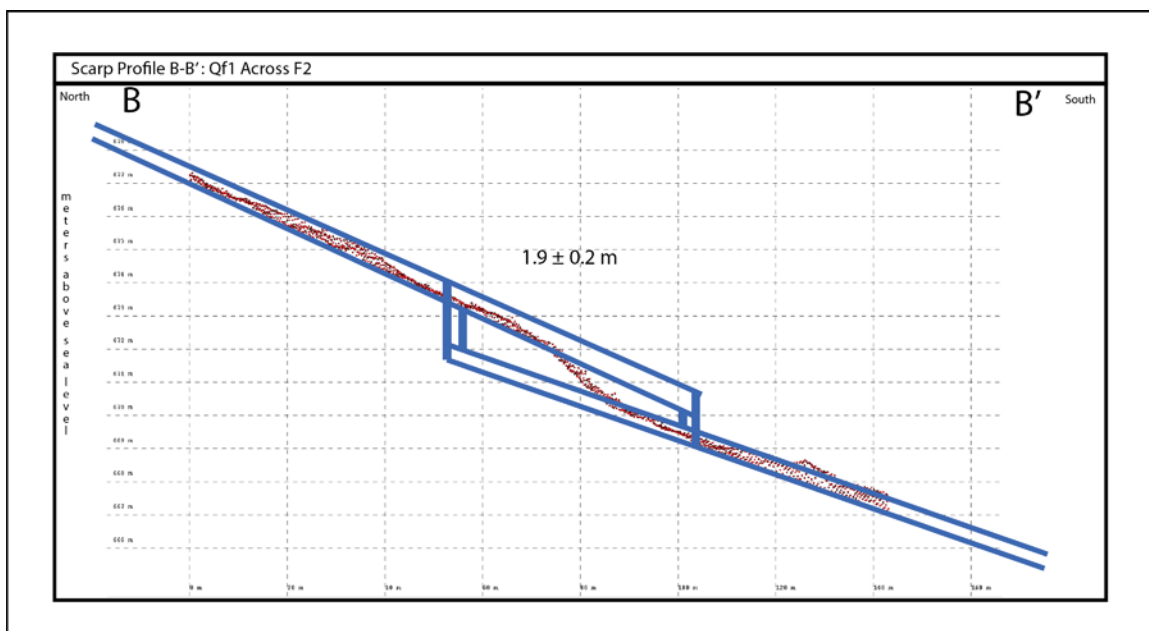
Camel Plot of Qf4 boulders. Curves represent smoothed frequency distribution of age data. Frequency overlap yields synergistic summation of probability thereby indicating the most probable age for the surface based on error range of each sample. Most probable age is indicated by highest peak of the summed kernel density estimate (Balco, 2008). Model was run in Matlab 2014 using CamelPlot code of Balco (2008). Mean weighted average (WMA) age for the Qf4 boulder suite is 6285 ± 330 years overlain in blue (ISOPLOT 4). I adopt the MWA for use in calculating age of Qf4 surface with Qf4 depth profile. Sample 1303-B1 (green); 1303-B2 (magenta); 1303-B3 (orange); 1303-B4 (yellow).

Figure 4.5a



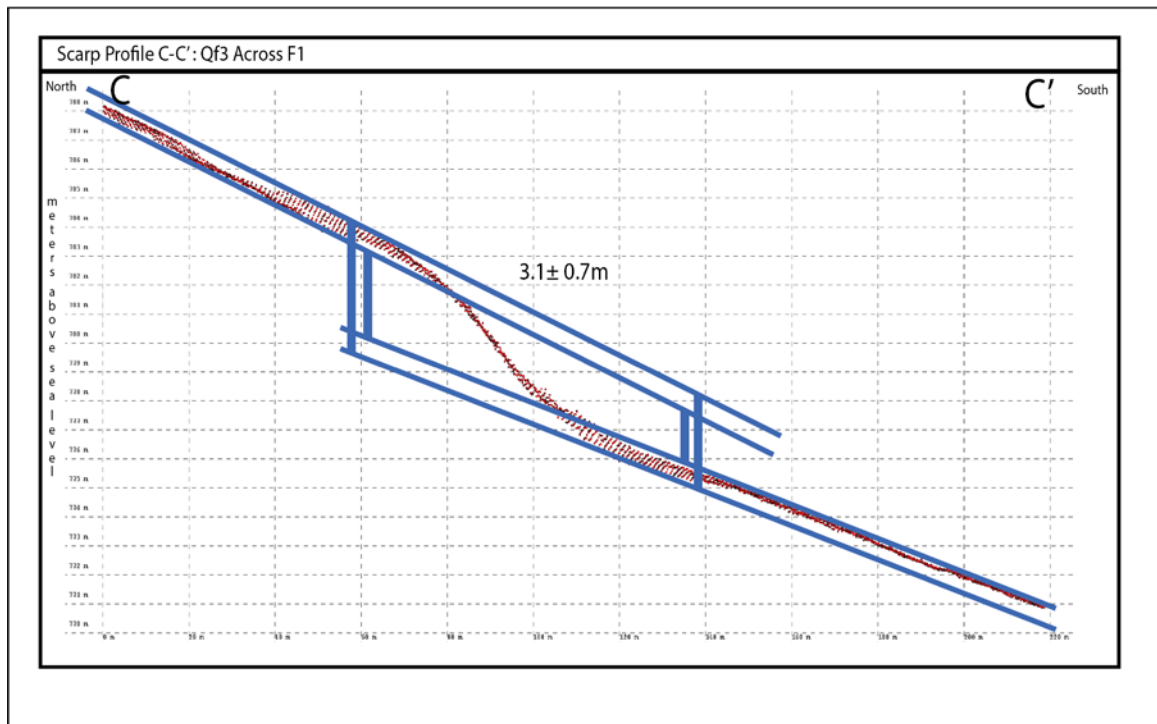
Fault F2 (southern) scarp, cross-sectional profile. Scarp preserves approximately 12.7 ± 1.4 meters vertical displacement of Qf4 surface. Profile obtained from B4 LiDAR dataset using QT Modeler software suite version 8.02. Cross section swath width set to 10 m.

Figure 4.5b



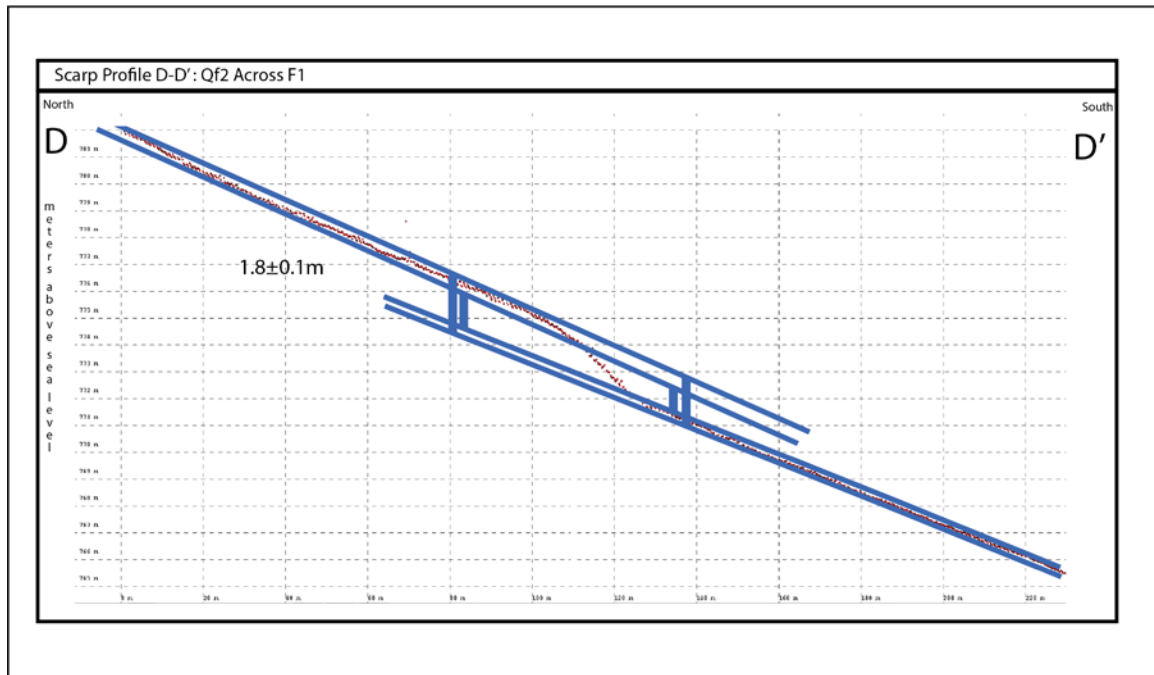
Fault F2 scarp, cross-sectional profile. Scarp preserves approximately 1.9 ± 0.2 meters vertical displacement of Qf1 surface. Profile obtained from B4 lidar dataset using QT Modeler software suite version 8.02. Cross section swath width set to 2 meters.

Figure 4.5c



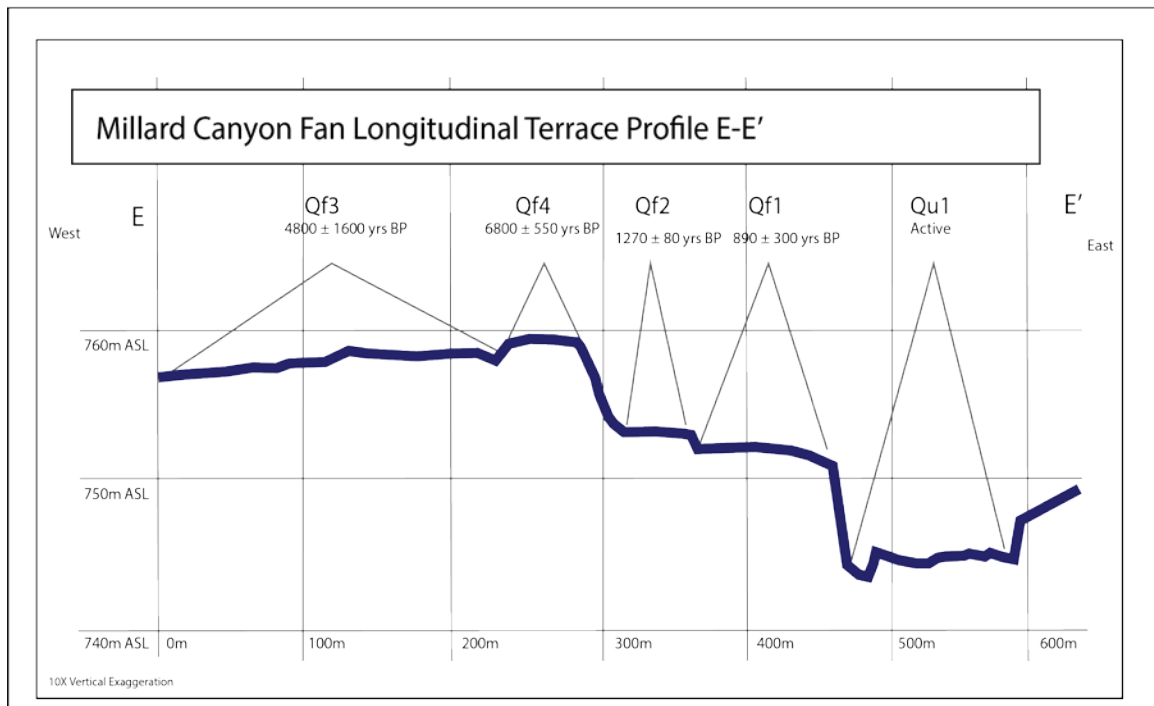
Fault F1 (upper) scarp, cross-sectional profile. Scarp preserves approximately 3.1 ± 0.7 meters vertical displacement of Qf3 surface. Profile obtained from B4 LiDAR dataset using QT Modeler software suite version 8.02. Cross section swath width set to 3 meters.

Figure 4.5d



Fault F1 (upper) scarp, cross-sectional profile. Scarp preserves approximately 1.8 ± 0.1 meters vertical displacement of Qf2 surface. Profile obtained from B4 LiDAR dataset using QT Modeler software suite version 8.02. Cross section swath width set to 3 meters.

Figure 4.6



Millard Canyon alluvial fan terrace cross-sectional profile. Figure shows surface ages for abandoned surfaces of erosional terraces. Profile obtained from B4 LiDAR dataset using QT Modeler software suite version 8.02. 10x Vertical exaggeration. Cross section swath width set to 1 meter.

Table 4.1

Fault	Surface	Age (years)	Dip Angle (degrees)	Uplift (meters)	Uplift Rate (mm/yr)	Dip Slip (meters)	Dip Slip Rate (mm/yr)	Contraction (meters)	Contraction Rate (mm/yr)
F2	Qf4	6800 ± 550	25	12.7 ± 1.4	1.86 ± 0.3	30 ± 3.3	4.4 ± 0.6	27.2 ± 3.0	4.0 ± 0.5
	Qf1	890 ± 300	25	1.9 ± 0.2	(-)	4.5 ± 0.5	(-)	4.1 ± 0.4	(-)
F1	Qf3	4800 ± 1600	45	3.1 ± 0.7	(-)	4.4 ± 1.0	(-)	3.1 ± 0.7	(-)
	Qf2	1270 ± 80	45	1.8 ± 0.1	1.4 ± 0.1	2.5 ± 0.1	2.0 ± 0.1	1.8 ± 0.1	1.4 ± 0.1

(-) Rates not calculated using these surfaces due to insufficient age constraints imparting large uncertainty to calculations.

Uncertainty Calculations made using quadratic methods as shown in Appendix C

Dip angles shown were used in calculations and are best estimate from available sources. Actual fault dip angles may vary up to 15 degrees.

Ages for Qf4 determined in this study; Qf2 from McBurnett (2011); Qf3 from constraint between Qf4 and Qf2 of McBurnett;

Qf1 interpreted from lower age limit of Qf2 and field relationships observed by Yule and Sieh (2003).

Summary of kinematic results from application of new cosmogenic age dating of Qf4, and mensuration of scarp heights using B4 LiDAR dataset. To simplify iterative calculations requiring complex quadratic propagation of uncertainty and to aid discussion, a single dip angle for each fault was used in this study. These dip angles are described by Yule and Sieh (2003) and originate from field observations and sidewall exposures in and near Millard Canyon. Actual in situ dip angles may vary by an estimated ± 10 degrees. Kinematic deformation is measured and calculated for all scarp surfaces, however only rates were calculated using surface ages with acceptable uncertainty. See discussion (section 6) for interpretation of these kinematic rates into net slip and potential per earthquake event motion.

Figure 5.1

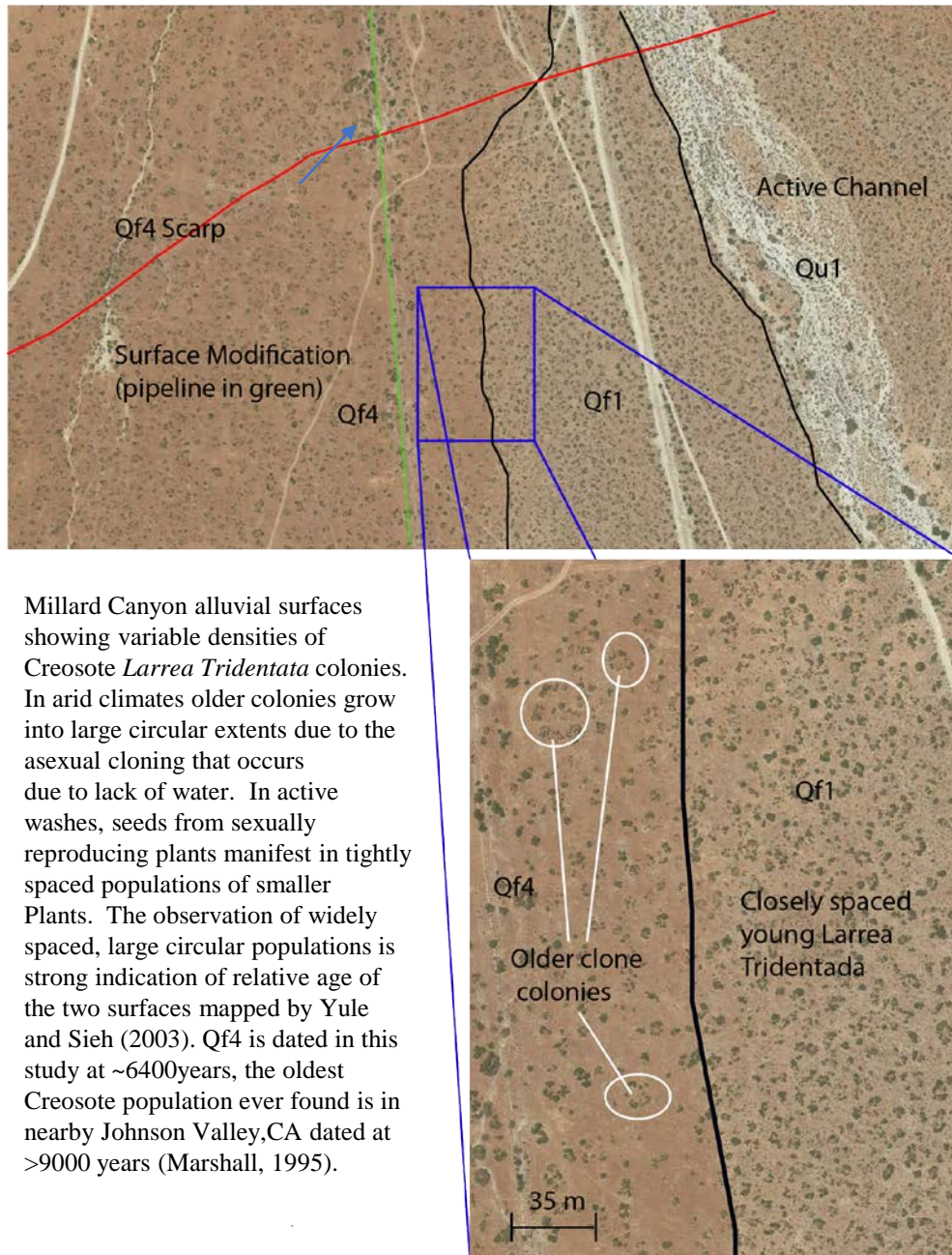
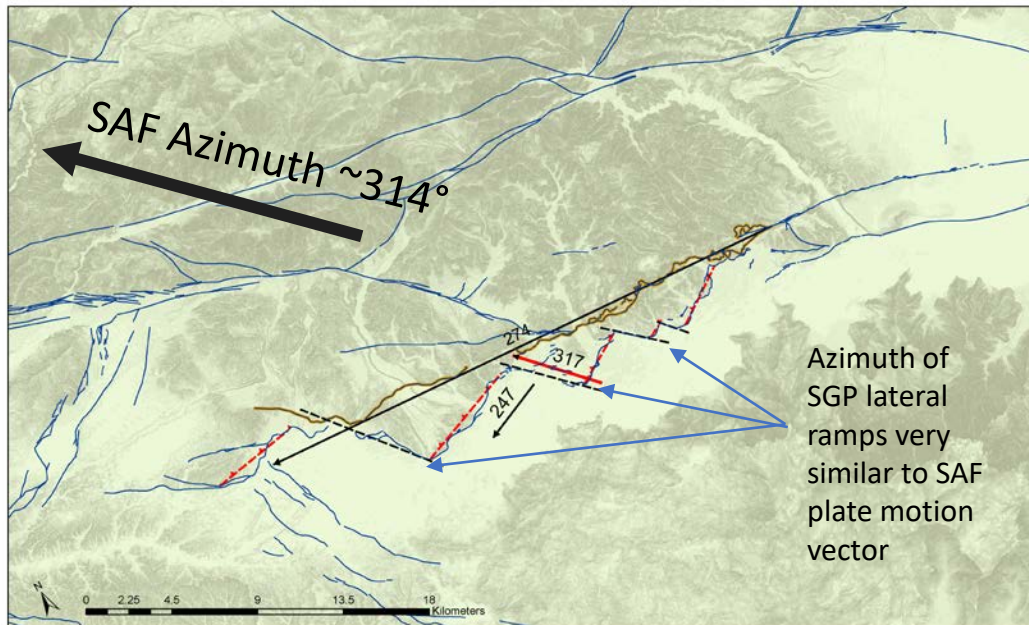
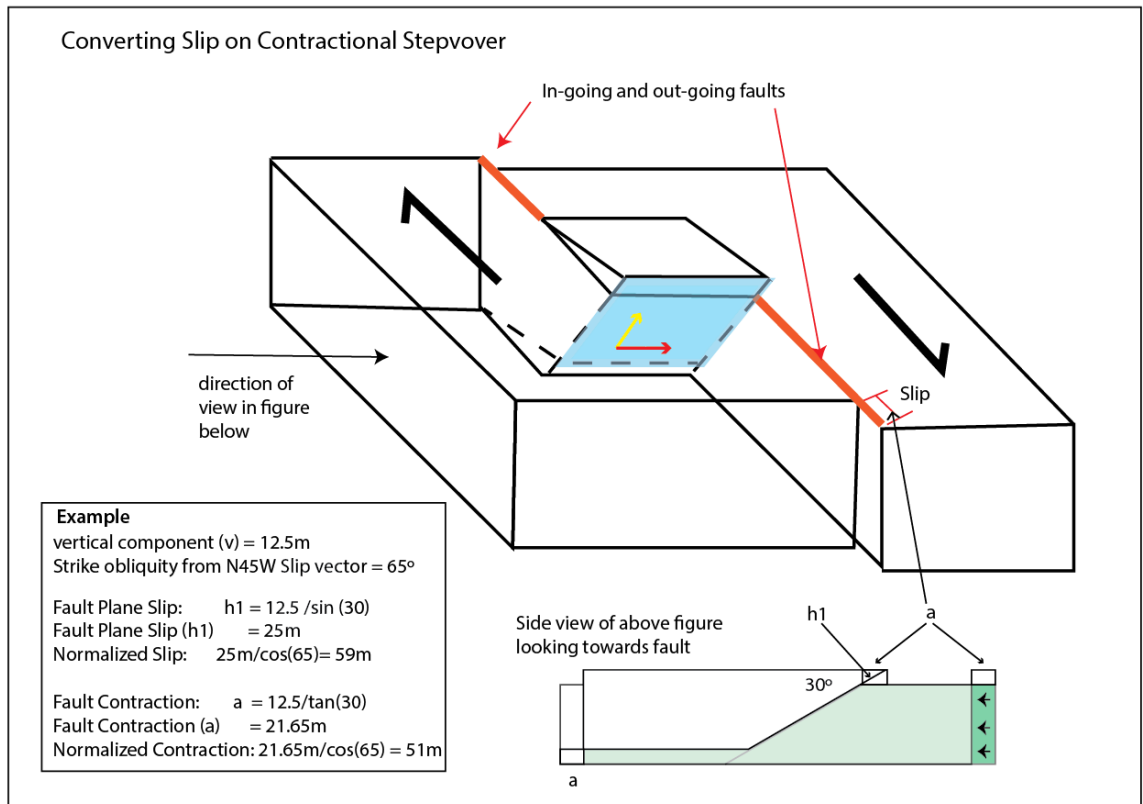


Figure 6.1



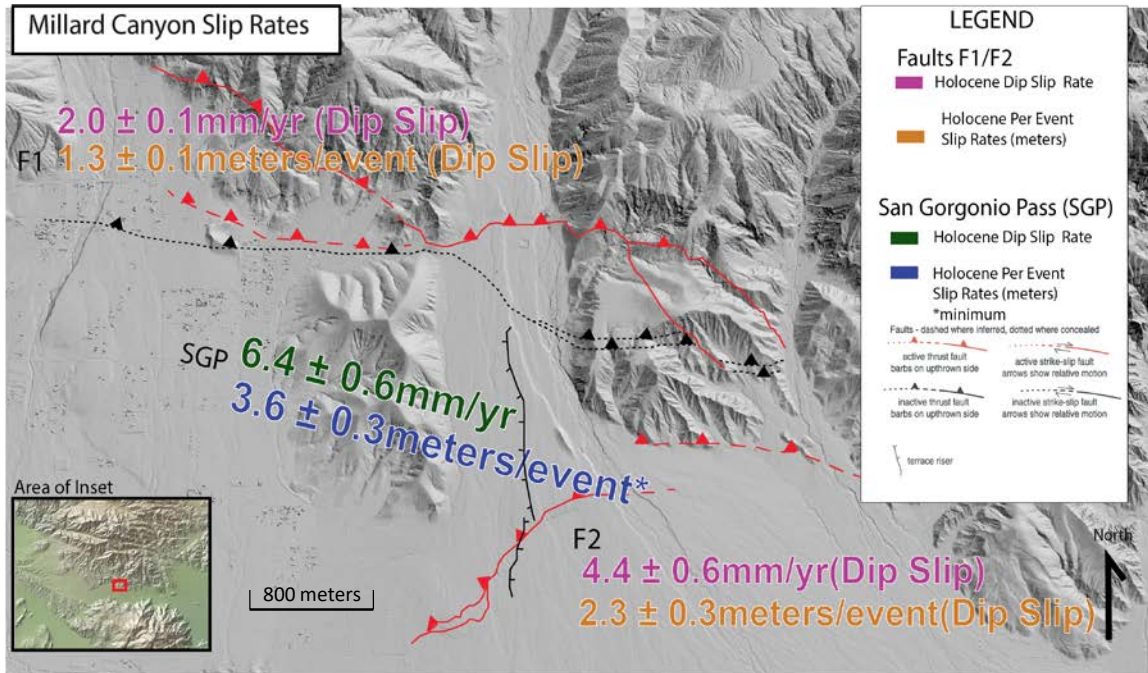
View of San Geronio Pass with overlay of USGS Quaternary fault Dataset. Analysis of fault trace trends using ESRI ArcGIS 10.3 “Mean Line Azimuth” geoprocessing tool, in WGS 84 Spheroid provides fault trace azimuths. Banning Strand SAF in orange with azimuth of 274°. San Geronio Pass Thrust, an active reverse tear fault, is represented with lateral ramps As black dashed lines, and frontal ramp as red dashed lines with teeth on upward moving block. Strike of Banning Strand is ~40° oblique from the N45W strike of the SAF transform plate boundary. This magnitude of obliquity still allows for strike slip transfer along a continuous fault plane. The Frontal ramps of the SGPT are 70° oblique from the N45W plate boundary slip vector. This magnitude Of obliquity indicates that the contractional slip occurring on the SGPT must be transferred via discontinuous and likely very complicated paths

Figure 6.2



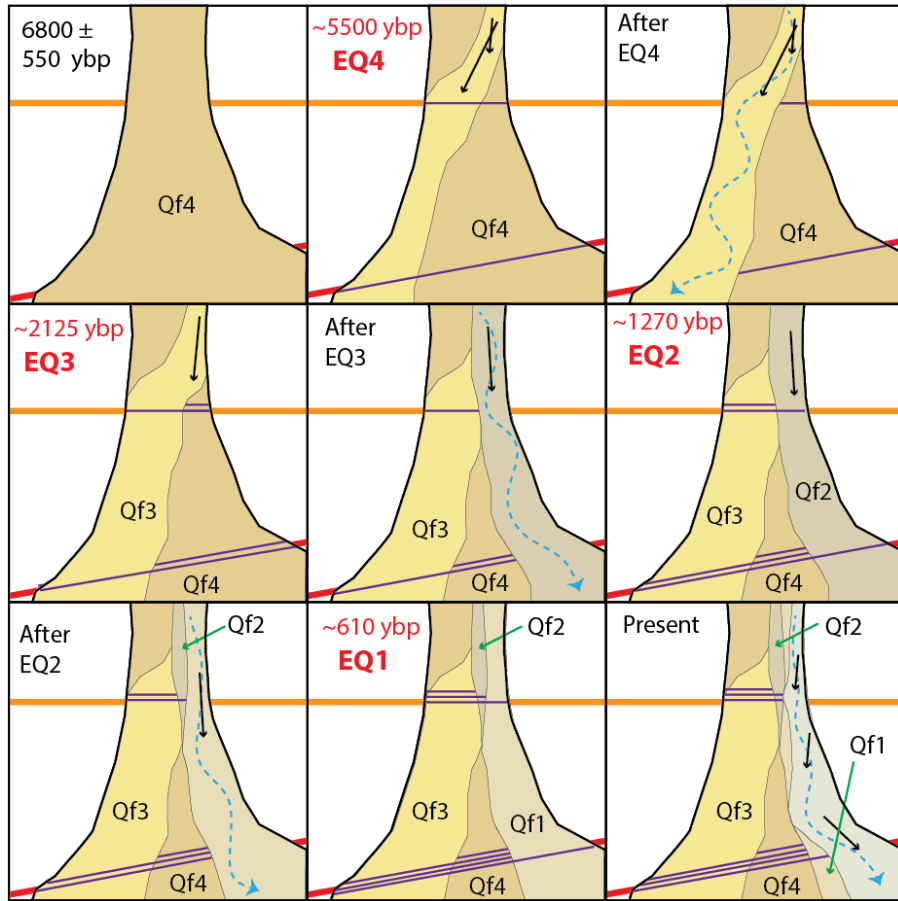
Schematic figure showing simplified geometry explaining conversion of contractional Components in a stepover area into strike slip on lateral ramps. The SGPT is interpreted to be a contractional left stepover comprised of a series of tear faults. These tear faults do not share a continuous fault plane and therefore are not a likely mechanism of slip Transfer through SGP. The deformation recorded in Millard Canyon and interpreted in this study are recording uplift and contraction on a low angle thrust fault. Analysis of surface trends of the SGPT shows the azimuth of the lateral ramps to be parallel to the 314° azimuth of the plate transform boundary. Therefore, any strike slip along this azimuth does not need to be trigonometrically projected onto the SAF slip vector (314°).

Figure 6.3



San Gorgonio Pass slip rates through Millard Canyon. Lower fault (F2) offset of Qf4 provides slip rates by resolving vertical uplift on a 30 degree North dipping fault. Upper fault (F1) provides slip rates by resolving vertical uplift onto 45 degree north dipping fault (reactivated Banning Strand SAF). Summation of these rates provides slip rate for SGP region for the Holocene and late Pleistocene (in green and blue). *These rates are minimums as only the dip slip component was calculated in this study. Yule and Sieh (2003) observe a strike slip to dip slip ratio on F1 of 1.8:1. This would yield a net slip per event rate of ~3 meters per event on F1.

Figure 6.4



Schematic interpretation showing geomorphic evolution of Millard Canyon surfaces through time with cumulative imprint of (what may an incomplete) paleoseismic record obtained from nearby trenching activities (McBurnett, 2011; Wolf et al., in progress). Model assumes contemporaneous rupture on northern and southern faults, however this behavior has not been proven to occur. Ruptures represented as purple lines, showing earthquakes 1-4. Disappearance of line illustrates erosion of scarp due to fluvial processes in active channel. Black arrows illustrate suspected direction of hydrologic forces pertinent to fluvial geomorphology of channel. Text in red designates the time frame in which the earthquake occurred. Qf1, Qf2, Qf3, Qf4; faulted alluvium; Q; undifferentiated. See figure 6 of Yule and Sieh (2003) for detailed geologic map.

Appendix C - Formulas Used

Formula 1. Standard Deviation Uncertainty Formula

$$\sigma = \sqrt{\frac{\sum_{i=1}^N (X_i - \bar{X})^2}{N - 1}} = \sqrt{\frac{(X_1 - \bar{X})^2 + (X_2 - \bar{X})^2 + \dots + (X_N - \bar{X})^2}{N - 1}}$$

Formula 2. Multiplication of Values with uncertainty

$$\Delta q = q_{best} \cdot \sqrt{\left(\frac{\Delta x}{x_{best}}\right)^2 + \left(\frac{\Delta y}{y_{best}}\right)^2}$$

Formula 3. Trigonometric Conversions

3a. Dip Slip (ds) = $throw/\sin(\theta)$

3b. Contraction = $throw/\tan(\theta)$

where

(θ) = fault dip angle (in degrees)

throw = measured vertical displacement across scarp (in meters)

Formula 4. Kernal Density Estimate Formula

(Extracted from Matlab Script of Balco, 2001)

$$y = \frac{1}{\sqrt{2\pi\sigma^2}} \exp \left[\frac{-(x - \mu)^2}{2\sigma^2} \right]$$

Formula 5. Aluminum/Beryllium Burial Dating

(From Balco and Rovey, 2008)

See reference for overview of variables.

$$N_{10,m} = \frac{P_{10}(0)}{\lambda_{10} + \frac{\epsilon}{\Lambda}} e^{-\lambda_{10}t_b} + \frac{P_{10}(z_b)}{\lambda_{10}} [1 - e^{-\lambda_{10}t_b}]$$

$$N_{26,m} = \frac{P_{26}(0)}{\lambda_{26} + \frac{\epsilon}{\Lambda}} e^{-\lambda_{26}t_b} + \frac{P_{26}(z_b)}{\lambda_{26}} [1 - e^{-\lambda_{26}t_b}]$$

$$R_m = \frac{N_{26,m}}{N_{10,m}} = \frac{P_{26}(0)}{P_{10}(0)} e^{-t_b(\lambda_{26} - \lambda_{10})}$$